Cyclostationarity of Communication Signals in Underwater Acoustic Channels

François-Xavier Socheleau

Cyclostationarity of Communication Signals in Underwater Acoustic Channels

François-Xavier Socheleau

Abstract

The effect of underwater acoustic propagation on the cyclostationary features of communication signals is modeled and analyzed. Two kinds of channels are considered: the multiscale-multilag channel, over which mobile and wideband acoustic systems usually communicate, and the dispersive channel resulting from low-frequency modal propagation in shallow water. It is shown that multiscale-multilag channels transform cyclostationary signals into a sum of velocity and acceleration-dependent time-warped cyclostationary processes. This time-warping is carefully taken into account to efficiently recover the cyclostationary features. On the other hand, it is found that low-frequency dispersive channels preserve the original periodicity but attenuate the shorter cycles and spread the correlations. To illustrate the theoretical results, applications with simulated and real data are also presented. Specifically, the problem of estimating time-varying Doppler scales is addressed for multiscale-multilag channels as well as the detection of signals with unique cyclostationary signatures. The example of blind symbol-rate estimation applied to covert communications in dispersive channels is also discussed. Special attention is paid to PSK, QAM, OFDM and DSSS signals. Accompanying supplementary material provides the MATLAB code used for the estimation and detection examples.

Index Terms

Acoustic communications, cyclostationarity, modal dispersion, multiscale-multilag channel, underwater warfare.

F.-X. Socheleau is with IMT Atlantique, Lab-STICC, France (e-mail: fx.socheleau@imt-atlantique.fr)

A preliminary version of this paper was presented at the Conference on Underwater Communications and Networking (UComms) in August 2021 [1].

I. INTRODUCTION

Communication signals are random and unpredictable by definition. However, due to repetitive pulse shaping, periodic carriers, framing or coding, they usually involve periodic processes in combination with their random fluctuations. Although not themselves periodic functions of time, communication signals often exhibit statistical characteristics that do vary periodically. They belong to the set of so-called cyclostationary (CS) processes [2]. Analysis of CS signals relies on a well-established theory which extends most signal processing tools historically developed for stationary signals [3], [4]. Such a theory mainly seeks to model, reveal and exploit the hidden periodicities (also called "cycles") of CS signals so as to extract relevant information. Cyclostationarity has found many applications in wireless communications such as signal detection, modulation classification and parameter estimation, source localization, interference mitigation or blind channel estimation, to name a few [2], [5]. CS-based algorithms offer several interesting properties. Like all statistics-based methods, they require little prior knowledge on the signal to process and "*are potentially immune to the effects of noise and interference, provided that a sufficiently long observation interval is adopted to estimate the cyclic statistics*" [5].

Although very popular in the context of terrestrial RF communications, CS-based methods have received little attention in the literature dedicated to underwater acoustic communications (UAC). Examples of UAC-specific contributions include Doppler scale estimation [6], [7], symbol rate estimation [8] and blind modulation classification [9]. However, these works apply and test RF methods with little adaptation to the specific features of underwater channels. For instance, they all assume that the motion-induced Doppler effect causes a constant time compression/dilation of the received signal over some (possibly short) measurement interval. As illustrated latter in this paper, such an assumption may be violated in high-mobility scenarios.

The main contribution of this paper is to model and analyze the effect of UAC channels on the second-order CS features of communication signals. We also develop CS-based algorithms that take into account "by design" the channel specificities. More precisely, we consider two UAC-specific channels, namely the multiscale-multilag (MSML) channel and the dispersive channel. Underwater MSML channels are observed in multipath propagation environments when the transmission bandwidth is of the same order as the carrier frequency and when the relative

velocity between the transmitter and receiver is non-negligible relative to the speed of sound [10]. In this scenario, the Doppler-shift approximation is no longer valid because the motion-induced Doppler effect actually compresses or dilates signals in time. This phenomenon is referred to as Doppler scaling. In addition, depending on the channel geometry, each path may experience a different Doppler scale, hence the name MSML channel. MSML models are not relevant for all communication scenarios. More specifically, at low frequency (a few hundreds of Hz) and in shallow water environments, the propagation is better described by normal-mode theory, which models the channel as the sum of several modes [11]. In such a scenario, each mode has its own travel time and bandwidth and the modal group velocity is frequency dependent so that the channel is said to be dispersive [12]. In other words, the propagation speed varies with frequencies and the usual model with individual paths is not accurate in this context. As discussed in the sequel, MSML and dispersive channels do not impact the cyclostationary features of UAC signals in the same way. MSML channels transform periodic statistics into velocity and acceleration-dependent time-warped statistics, whereas dispersive channels keep the original periodicity but attenuate the shorter cycles and spread the correlations.

To promote the use of CS-based method in UAC contexts and illustrate the theoretical results, applications with both simulated and real data are also presented. Two experiments are conducted in MSML channels and one in a dispersive channel.

1) In the first experiment, the estimation of time-varying Doppler scales resulting from strong accelerations is considered. A method capable of estimating multiple Doppler scales, as observed in MSML channels, is proposed and assessed on simulated PSK/QAM signals. This method takes advantage of the CS features that become time-warped as a result of Doppler scaling. More specifically, a quadratic function of time is used to model the motion-induced Doppler and a cost function is derived based on the autocorrelation properties. This cost is then iteratively optimized to estimate the polynomial coefficients related to the velocity and acceleration of each path. The estimation procedure is non-data-aided. It does not affect the data rate and is applicable in non-cooperative scenarios.
2) The second application deals with the problem of detecting a UAC signal with a specific CS signature. Such a signature may be unique and therefore relevant to detect a given communication system in underwater warfare-like applications. A statistical test that explicitly considers time-varying Doppler scales is derived. This test offers reasonable

complexity and its performance is illustrated with real CP-OFDM data collected in shallow-water MSML channels. It is shown to provide much better performance than off-the-shelf RF methods.

3) The last experiment is dedicated to the problem of blind symbol-rate estimation applied to a DSSS transmission in a dispersive channel. Such a problem may be of key importance for eavesdropping on low-frequency covert communications. As opposed to MSML channels, dispersive channels do not distort much the CS features so that estimators already available in the literature require little adaptation. An estimator is presented and its performance is illustrated with replay simulations using real low-frequency single-input mutliple-output (SIMO) shallow-water impulse responses. It is shown that the spatial coherence along the array results in a significant improvement in correct estimation rate.

The Matlab code of these examples is provided as supplementary material [13].

The rest of this paper is organized as follows. Concepts and definitions related to the second-order cyclostationarity of communications signals are reviewed in Section II, with emphasis on PSK/QAM, OFDM and DSSS signals. The impact of MSML channels on CS features is modeled, analyzed and illustrated in Section III. A Doppler-scale estimator and a CS detector are derived in Section III-C and III-D, respectively. The effect of dispersive channels with application to blind symbol-rate estimation of DSSS signals is presented in Section IV. Finally, conclusions are drawn in Section V.

II. Cyclostationarity of communication signals

A. General definitions

A random signal $x(t)$ is said to be second-order cyclostationary (CS) in the wide sense if its mean and autocorrelation are periodic functions of time [2]. More specifically, let $R_x(t,u)$ be the autocorrelation function defined as

$$R_x(t,u) \triangleq \mathbb{E}\left\{x^*(t)x(t+u)\right\}. \tag{1}$$

If $x(t)$ is second-order cyclostationary with period $T_0 > 0$, $R_x(t,u)$ admits the following Fourier series expansion

$$R_x(t,u) = \sum_{\alpha\in\mathcal{A}} R_x^\alpha(u) e^{i2\pi\alpha t}, \tag{2}$$

where $\mathcal{A} = \{k/T_0\}_{k\in\mathbb{Z}}$ denotes the countable set of cycle frequencies α and $R_x^\alpha(u)$ is the cyclic autocorrelation function defined as

$$R_x^\alpha(u) \triangleq \frac{1}{T_0}\int_{-\frac{T_0}{2}}^{\frac{T_0}{2}} R_x(t,u)e^{-i2\pi\alpha t}\mathrm{d}t. \tag{3}$$

For each $\alpha \in \mathcal{A}$, let

$$S_x^\alpha(\nu) \triangleq \int_{\mathbb{R}} R_x^\alpha(u)e^{-i2\pi u\nu}\mathrm{d}u \tag{4}$$

referred to as the cyclic spectrum. This spectrum reveals the spectral correlation of CS signals. More precisely, CS signals have correlated spectral components when the frequency difference is equal to a cycle frequency, that is [2]

$$S_x(\nu_1,\nu_2) \triangleq \mathbb{E}\{X^*(\nu_1)X(\nu_2)\} = \sum_{\alpha\in\mathcal{A}} S_x^\alpha(\nu_2)\delta(\nu_1-\nu_2+\alpha), \tag{5}$$

where $\delta(\cdot)$ denotes the Dirac delta distribution, $X(\nu)$ is the Fourier transform of $x(t)$ and $S_x(\nu_1,\nu_2)$ is called the spectral correlation function (or Loève bifrequency spectrum). As discussed in Sec. III and IV, the choice to study the cyclostationary properties in time via the autocorrelation function or in frequency via the spectral correlation function will depend on the characteristics of the considered channel.

B. Examples

Most communication signals are cyclostationary with a period equal to the symbol period T_s. This is illustrated in Fig. 1 with the cyclic autocorrelation function of four types of signals commonly used in underwater acoustic communications: PSK/QAM [14], [15] (top left), short-code DSSS [16]–[18] (top right), cyclic prefix OFDM (CP-OFDM) [19]–[21] (bottom left), and guard-free OFDM with super-imposed pilots (SIP-OFDM) [22] (bottom right). Each signal has its own CS pattern, which can be useful for blind modulation recognition, and each pattern reveals the value of the symbol period T_s. As further discussed and illustrated in Appendix A, such signals exhibit periodic second-order statistics due to the repetitive use of the same pulse-shaping filter, same spreading or pilot sequence, or due to the redundancy induced by a cyclic prefix. Other types of UAC waveforms such as MFSK, frequency-hopped FSK (as used in the JANUS standard [23]), or chirp spread-spectrum are also second-order CS [24], [25]. Although not discussed in this paper, the examples of applications presented in the next sections could easily be transposed to these non-coherent modulation schemes. Finally, in addition to

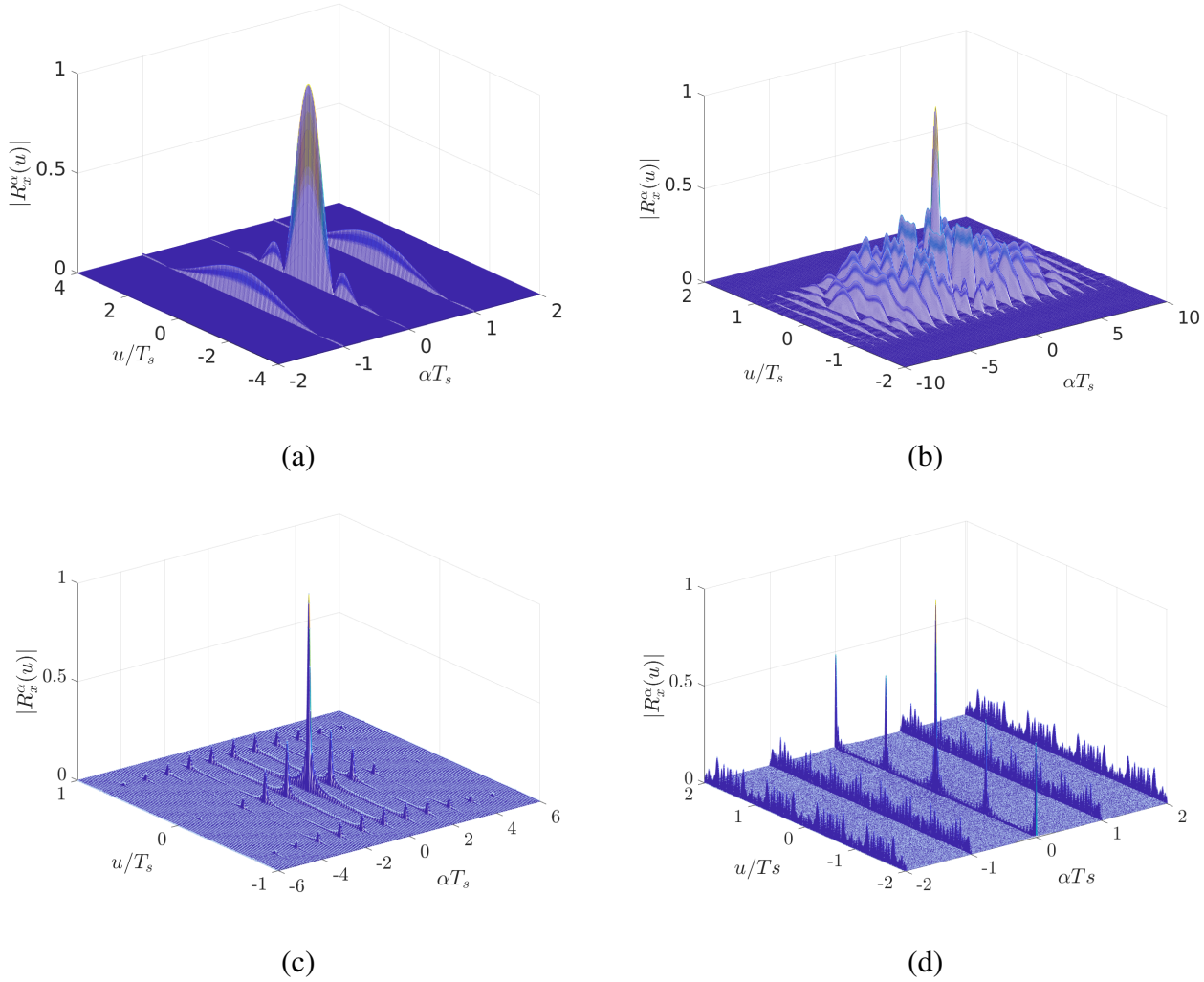

Fig. 1: Examples of cyclic autocorrelation functions. (a) PSK/QAM with a root-raised-cosine filter, (b) short-code DSSS with a 7-chip long spreading sequence and a root-raised-cosine filter (c) CP-OFDM with a root-raised-cosine window, (c) SIP-OFDM with a rectangular window

data symbols, UAC signals often include signaling patterns such as preambles, postambles, or time-frequency pilots that can generate additional CS features [26], [27]. In that case, the cycle frequencies can be incommensurate and the signal is said to be *almost* CS [4]. In order not to depend on a particular frame structure, the methods presented in the rest of the paper only take advantage of the information provided by the cycle frequencies which are multiples of the symbol rate.

III. Cyclostationarity in multiscale-multilag channels

A. Channel model

As mentioned previously, MSML channels are observed in wideband, mobile and multipath propagation environments. Given an input CS signal $x(t)$, the channel output $r(t)$ satisfies [1]

$$r(t) = \sum_{\ell=1}^{L} \lambda_\ell(t) y_\ell(t) + w(t), \tag{6}$$

where $\lambda_\ell(t)$ is the random complex attenuation of the ℓ-th channel tap and $w(t)$ is the additive noise assumed to be wide-sense stationary. In practice, the received signal is observed over a finite duration T_{obs}, which, as illustrated in Sec. III-C, is on the order of a few seconds or less. Over that duration, the time-varying impulse response can be reasonably approximated as wide-sense stationary (WSS) [28]–[30] so that $\mathbb{E}\left\{\lambda_\ell^*(t)\lambda_m(t+u)\right\} = R_{\lambda_\ell,\lambda_m}(u)$ does not depend on t. In (6), the signal $y_\ell(t)$ is a delayed, phase and frequency shifted as well as time-warped version of the transmitted signal, i.e.,

$$y_\ell(t) \triangleq x(\psi_\ell(t) - \tau_\ell) e^{i2\pi f_c(\psi_\ell(t) - \tau_\ell - t)}. \tag{7}$$

τ_ℓ denotes the initial time of arrival of the ℓ-th tap, f_c is the carrier frequency and $\psi_\ell(t)$ is the time-varying delay of the ℓ-th tap. Stated differently, $\psi_\ell(t)$ is the time-warping function of the ℓ-th tap resulting from motion-induced Doppler scaling. Each function $\psi_\ell(t)$ is usually modeled as the sum of a dominant term, compensated by resampling at reception, plus some residual Doppler shift that can be tracked with narrowband processing. We here focus on the dominant term and model the relative motion between the transmitter (TX) and the receiver (RX) with the following polynomial [31, Eq. (9)]

$$\psi_\ell(t) \triangleq \left(1 - \frac{v_\ell}{c}\right) t - \frac{a_\ell}{2c} t^2 + o(t^2), \tag{8}$$

where c is the sound speed, v_ℓ is the relative velocity between TX and RX, and a_ℓ is the relative acceleration. In typical underwater scenarios, c is usually around 1500 m.s^{-1}, v_ℓ is on the order of a few meters per second and a_ℓ is bounded by a couple a meters per second squared. Model (8) is usually relevant only if the observation window is restricted to a few seconds or less. Fig. 2 shows an example of the motion-induced time-varying delays of a MSML channel simulated

[1]For the sake of simplicity, the frequency-dependent losses are voluntarily omitted in the channel model.

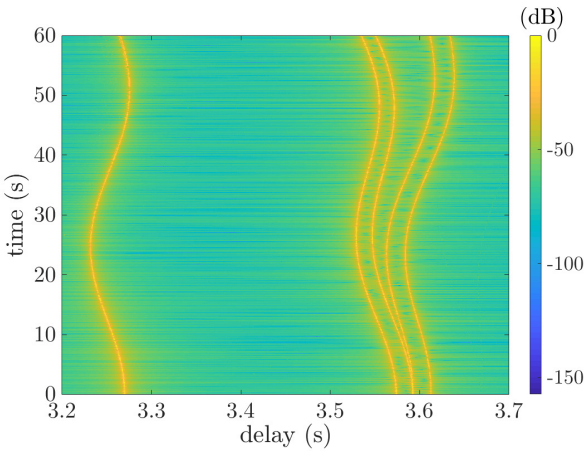

Fig. 2: Example of a simulated time-varying impulse response obtained with Bellhop. Kauai environment [32, Fig. 16], range varying between 4.97 and 5.03 km, TX depth = 50 m, RX depth varying between 50 and 200 m.

with Bellhop [32] over 60 seconds. Within any time interval of a few seconds, we see that a second-order approximation of the time-varying delays seems reasonable. However, in some specific environments such as the surf zone, note that Eq. (8) may not be accurate to model the possible effects of wave-induced Doppler on surface-reflected arrivals. As illustrated in [33], the acoustic focusing by the curvature of the wave crest can create time-varying delays with discontinuities. Such an environment is not considered in the present analysis.

B. Cyclostationary analysis

Although the transmitted signal $x(t)$ is CS, Doppler scaling expressed in (7) can destroy the cyclic feature of the received signal, i.e., $R_r(t,u)$ may not be periodic. However, each time-warped signal $y_\ell(t)$ shows interesting properties. More specifically, as shown in Appendix B,

$$R_{y_\ell}(t,u) = e^{i2\pi f_c(\phi_\ell(t,u)-u)} \times \sum_{\alpha\in\mathcal{A}} R_x^\alpha(\phi_\ell(t,u)) e^{i2\pi\alpha(\psi_\ell(t)-\tau_\ell)}, \tag{9}$$

where

$$\phi_\ell(t,u) \triangleq \psi_\ell(t+u) - \psi_\ell(t) = \psi_\ell(u) - uta_\ell/c. \tag{10}$$

Equivalently,

$$R_{y_\ell}(t,u) = e^{i2\pi f_c(\psi_\ell(u)-u)} \sum_{\alpha\in\mathcal{A}} R_x^\alpha(\phi_\ell(t,u)) e^{i2\pi\left(\alpha(\psi_\ell(t)-\tau_\ell)-\frac{a_\ell}{c}uf_ct\right)}. \tag{11}$$

Moreover, as illustrated in Sec. III-C and III-D, the correlation is always computed for a finite lag $|u| < u_{\max}$ and typical values for v_ℓ, a_ℓ, c, $u_{\max}$ and T_{obs} are such that

$$\sup_{(t,u)\in[0,T_{\text{obs}}]\times[-u_{\max},u_{\max}]} \left|\frac{\partial\phi_\ell(t,u)}{\partial u}\right| >> \sup_{(t,u)\in[0,T_{\text{obs}}]\times[-u_{\max},u_{\max}]} \left|\frac{\partial\phi_\ell(t,u)}{\partial t}\right|. \tag{12}$$

For instance, if $|v_\ell| \leq 10$ m.s^{-1}, $|a_\ell| \leq 3$ m.s^{-2}, $c = 1500$ m.s^{-1}, $|u_{\max}| = 0.1$ s and $T_{\text{obs}} \leq 1$ s, we have $\sup_{(t,u)\in[0,T_{\text{obs}}]\times[-u_{\max},u_{\max}]} \left|\frac{\partial\phi_\ell(t,u)}{\partial u}\right| \approx 1.009$ and $\sup_{(t,u)\in[0,T_{\text{obs}}]\times[-u_{\max},u_{\max}]} \left|\frac{\partial\phi_\ell(t,u)}{\partial t}\right| \approx 1.2\,10^{-4}$. Therefore, $\phi_\ell(t,u)$ can be closely approximated as $\phi_\ell(t,u) \approx \psi_\ell(u)$, which yields

$$R_{y_\ell}(t,u) \approx e^{i2\pi f_c(\psi_\ell(u)-u)} \times \sum_{\alpha\in\mathcal{A}} R_x^\alpha(\psi_\ell(u)) e^{i2\pi\left(\alpha(\psi_\ell(t)-\tau_\ell)-\frac{a_\ell}{c}uf_ct\right)}. \tag{13}$$

Eq. (13) reveals that Doppler scaling changes the periodic function of time $R_x(t,u)$ into a correlation function $R_{y_\ell}(t,u)$ made of a sum of chirp signals with velocity and acceleration-dependent time-varying phases. Such a process is known as a time-warped cyclostationary process [34], [35]. If the time-warping function $\psi_\ell(t)$ is known and invertible, the original cyclic feature can be restored. This is expressed by the following relationship

$$R_x^\alpha(u) = \lim_{T\to\infty} \frac{e^{i2\pi\alpha\tau_\ell}}{T} \int_{-\frac{T}{2}}^{\frac{T}{2}} \rho\left(\psi_\ell^{-1}(t), \psi_\ell^{-1}(t+u)\right) e^{-i2\pi\alpha t}\mathrm{d}t, \tag{14}$$

where $\rho(t,t+u) \triangleq R_{y_\ell}(t,u)e^{-i2\pi f_c(\phi_\ell(t,u)-u)}$ and where the expression of $\psi_\ell^{-1}(\cdot)$ is given in Eq. (82) (see Appendix B).

It follows that the autocorrelation function $R_r(t,u)$ of the received signal can be approximated as a linear combination of several chirp signals. That is,

$$\begin{aligned} R_r(t,u) &= \sum_{\ell=1}^{L}\sum_{m=1}^{L} \mathbb{E}\left\{\lambda_\ell^*(t)\lambda_m(t+u)\right\}\mathbb{E}\left\{y_\ell^*(t)y_m(t+u)\right\} + \mathbb{E}\left\{w^*(t)w(t+u)\right\} \\ &= \sum_{\ell=1}^{L}\sum_{m=1}^{L} R_{\lambda_\ell,\lambda_m}(u)R_{y_\ell,y_m}(t,u) + R_w(u), \end{aligned} \tag{15}$$

where, under Assumption (12),

$$R_{y_\ell,y_m}(t,u) = e^{i2\pi f_c(\psi_m(t+u)-\psi_\ell(t)+\tau_\ell-\tau_m-u)} \times \sum_{\alpha\in\mathcal{A}} R_x^\alpha(\psi_m(u)+\tau_\ell-\tau_m) e^{i2\pi\alpha(\psi_\ell(t)-\tau_\ell)}. \tag{16}$$

The effect of a MSML channel on the autocorrelation function is illustrated in Fig. 3 for a QPSK signal. We can see that $R_x(t,0)$ and $R_r(t,0)$ are in-phase at the beginning and then we can clearly observe the time-varying phase shift due to the time-warping functions $\psi_\ell(t)$. The double sum over taps in (15) also affects the amplitude of $R_r(t,0)$. Note that since the

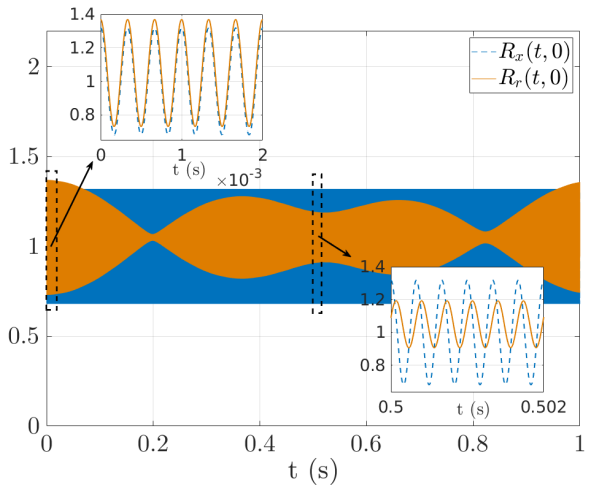

Fig. 3: Effect of the MSML channel of Figure 2 on the autocorrelation function of a QPSK signal. $T_s = 1/3$ ms, SNR = 20 dB, $u = 0$.

noise is assumed to be wide-sense stationary, it does not affect the time-varying phase of the autocorrelation function (15). It only increases the mean amplitude.

If we now switch to the frequency domain, it turns out that the spectral autocorrelation function (SAF) is not so relevant to analyze CS signals in MSML channels as it simply does not exist in the general case with $a_\ell \neq 0$.[2] It may be relevant only for scenarios where the acceleration can be neglected over the observation window. In this specific case and as shown in Appendix C, the SAF satisfies

$$\begin{aligned} S_r(\nu_1,\nu_2) \;=\; & \frac{c}{|c-v_\ell|}\sum_{\ell=1}^{L}\sum_{m=1}^{L}\sum_{\alpha\in\mathcal{A}} S^0_{\lambda_\ell\lambda_m}(\nu_2) \circledast S^\alpha_x\left(\frac{c\nu_2+f_c v_\ell}{c-v_\ell}\right) \\ & \times\delta\left(\nu_1-\frac{c-v_\ell}{c-v_m}\nu_2+\alpha\left(1-\frac{v_\ell}{c}\right)+f_c\frac{v_\ell-v_m}{c-v_m}\right) \\ & \times e^{i2\pi\frac{c(\tau_\ell-\tau_m)}{c-v_m}(\nu_2+f_c)} e^{-i2\pi\alpha\tau_\ell} \\ & + S^0_w(\nu_2)\delta(\nu_1-\nu_2), \end{aligned} \tag{17}$$

where $S^0_{\lambda_\ell\lambda_m}(\cdot)$ is the cross-spectral density (Doppler spectrum) of the channel taps and $S^0_w(\cdot)$ is the noise power spectral density. By comparing (5) and (17), we can notice that the support

[2]The process is said to be not harmonizable in the sense of Loève. See [34, Sec. III-A] for a detailed discussion on these aspects.

of $S_x(\nu_1, \nu_2)$ is made of lines with unit slopes in the bifrequency plane, whereas, at the output of the channel, there are additional lines with slopes $(c - v_\ell)/(c - v_m)$.

C. Application 1: Doppler scale estimation

As shown in Eq. (15) and illustrated in Fig. 3, the autocorrelation function of the received signal is a linear combination of several chirp signals with velocity and acceleration-dependent time-varying phases. We propose to take advantage of this property to estimate the time-warping functions $\psi_\ell(t)$ of the MSML channel. More precisely, given the observation $r(t)$, our objective is to estimate $\psi_\ell(t)$ (or, equivalently, v_ℓ and a_ℓ) without the knowledge of the transmitted symbols (non-data-aided scenario). This estimation is illustrated with PSK/QAM signals but, as discussed later, is applicable to any cyclostationary signal. We first consider a single Doppler scale scenario and then extend the estimator to multipath signals with different Doppler scales

1) Single-scale multilag channel: We here assume that the channel exhibits a single Doppler scale, i.e., $\psi_\ell(t) = \psi(t), \forall \ell$. Such an assumption may be reasonable in some shallow-water environments with a transmission range much greater than the water depth [36]. As illustrated in Fig. 1-(a), the cyclic autocorrelation function of PSK and QAM signals is maximized for $u = 0, \forall\, \alpha$. This suggests to estimate the time-warping function $\psi(t)$ based on the analysis of the zero-lag autocorrelation function of the received signal. More precisely, for $u = 0$, Eq. (15) simplifies to

$$R_r(t, 0) = \sum_{\ell=1}^{L} \sum_{m=1}^{L} R_{\lambda_\ell, \lambda_m}(0) R_{y_\ell, y_m}(t, 0) + R_w(0), \tag{18}$$

with

$$R_{y_\ell, y_m}(t, 0) = e^{i2\pi f_c(\tau_\ell - \tau_m)} \times \sum_{n=-1}^{1} R_x^{\frac{n}{T_s}}(\tau_\ell - \tau_m) e^{i2\pi \frac{n}{T_s}(\psi(t) - \tau_\ell)}. \tag{19}$$

Equivalently, by expanding the sums in (18) and (19), this autocorrelation function can be expressed as

$$R_r(t, 0) = 2\Re\left\{ A e^{i\frac{2\pi}{T_s}\psi(t)} \right\} + K, \tag{20}$$

where $A \in \mathbb{C}$ and $K \in \mathbb{R}$ denote time-invariant but signal and channel-dependent terms. Note that K also depends on the noise power. From Eq. (20), we see that the time-warping function $\psi(t)$ can be obtained by projecting $R_r(t, 0)$ onto a chirp basis, that is

$$\psi(t) = \underset{\varphi(t)}{\operatorname{argmax}} \left| \lim_{T \to \infty} \frac{1}{T} \int_{-\frac{T}{2}}^{\frac{T}{2}} R_r(t, 0) e^{-i\frac{2\pi}{T_s}\varphi(t)} \mathrm{d}t \right|^2. \tag{21}$$

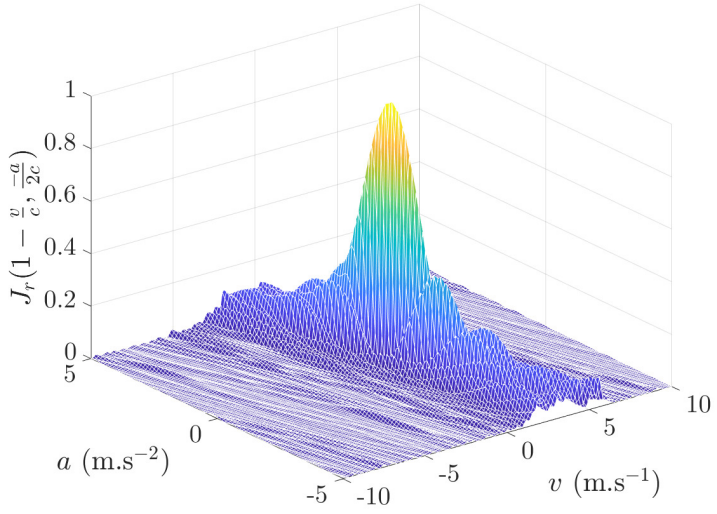

Fig. 4: Example of a cost function J_r obtained with a QPSK signal propagated in a shallow-water channel using a time-varying simulation with Bellhop [32]. $T_{obs} = 1$ s, $T_s = 0.2$ ms, $f_c = 20$ kHz, $E_b/N_0 = 7$ dB, $c = 1500$ m.s^{-1}, $v = 1$ m.s^{-1}and $a = 0.5$ m.s^{-2}.

In practice, we only observe a single realization of the received signal so that $R_r(t,0) = \mathbb{E}\{|r(t)|^2\}$ cannot be computed. However, $\widehat{R_r}(t,0) = |r(t)|^2$, which is an unbiased estimate of $R_r(t,0)$, can easily be computed. Moreover, since Doppler scaling is due to relative motion, the polynomial model (8) can be used. Therefore, over some time interval T_{obs} and by assuming that T_s is known, $\psi(t)$ can be estimated as

$$\widehat{\psi}(t) = \widehat{\mu}_1 t + \widehat{\mu}_2 t^2 \text{ with } (\widehat{\mu}_1, \widehat{\mu}_2) = \underset{(\mu_1,\mu_2)}{\text{argmax}}\, J_r(\mu_1,\mu_2) \tag{22}$$

and

$$J_r(\mu_1,\mu_2) = \frac{1}{T_{\text{obs}}} \left| \int_0^{T_{\text{obs}}} |r(t)|^2 e^{-i\frac{2\pi}{T_s}(\mu_1 t + \mu_2 t^2)} \mathrm{d}t \right|^2 . \tag{23}$$

An example of the cost function J_r is shown in Fig. 4. Given the shape of this function, the optimization can be done by first performing a coarse-grid search and by then applying a gradient approach. Details on the implementation of the estimator (22) are provided in Appendix D.

To illustrate the performance of the cyclostationary-based estimator (CSB), we consider a shallow-water channel with a constant sound speed profile with $c = 1500$ m.s^{-1}. The water, TX and RX depths are set to 50, 10 and 35 m, respectively. The initial transmit range is

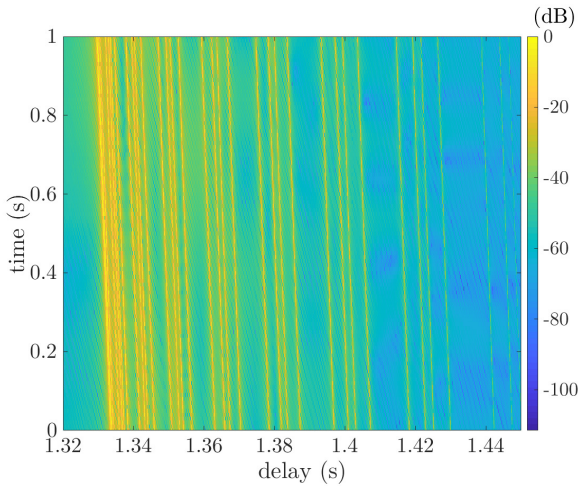

Fig. 5: Example of a simulated shallow-water time-varying impulse response obtained with Bellhop, $v = -6.1$ m.s^{-1} and $a = 0.5$ m.s^{-2}.

set to 2 km. root-raised-cosine (RRC) filtered QPSK signals are simulated with $T_{obs} = 1$ s, $T_s = 0.2$ ms, $f_c = 20$ kHz, a roll-off set to $\xi = 0.25$ and a (baseband) sampling rate of 20 kHz. The TX moves horizontally with radial velocity and acceleration randomly drawn from the set $[-v_m, v_m] \times [-a_m, a_m]$, with $v_m = 10$ m.s^{-1} and $a_m = 1$ m.s^{-2}. Bellhop is used to model the time-varying multipath distortions due to relative motion. 100 Bellhop impulse responses per second are generated along the TX/RX trajectory. These impulse responses are then linearly interpolated in time to match the sampling frequency of the transmitted signal. An example of shallow-water impulse response is shown in Fig. 5.

Our method is compared with [31]. This method, known as the "Multibranch Autocorrelation" (MBA), is able to estimate the velocity as well as the acceleration for systems using periodic pilot signals or repetitive data transmission. We here consider the first configuration applied to QPSK signals. In this case, the in-phase component is dedicated to periodic pilot transmission and the quadrature one to data [37]. The pilot sequence is 0.5 s long and is repeated twice. The receiver does not know the value of the pilot symbols but exploits the redundancy between consecutive blocks. As opposed to our approach, this method reduces the useful data rate by 2. However, note that pilots can also be used for time synchronization or to estimate the channel and the SNR, which is not considered in this paper. We use the root mean squared error (RMSE)

of the estimate $\widehat{\psi}(t)$ as our performance metric. It is defined as

$$\text{RMSE} = \sqrt{\frac{\mathbb{E}\left\{\int_0^{T_{obs}} \left(\widehat{\psi}(t) - \psi(t)\right)^2 \mathrm{d}t\right\}}{\mathbb{E}\left\{\int_0^{T_{obs}} \psi^2(t)\mathrm{d}t\right\}}}. \tag{24}$$

Fig. 6 shows the estimated RMSE for both methods as a function of E_b/N_0, where E_b is the signal energy per information bit and N_0 is the power spectral density of the additive white Gaussian noise. RMSE is estimated with 300 Monte-Carlo trials per E_b/N_0. As a reference, the RMSE of the dummy estimator $\widehat{\psi}(t) = t$ is also plotted. The parameters of method [31] are set as explained in [37, Sec. IV]: delay step=50 μs and frequency step = 1 Hz. The solution of (22) is found by first applying a coarse grid search with a step of $1/9.10^{-3}$ for μ_1 and $1/6.10^{-3}$ for μ_2. This corresponds to a step of 1/6 m.s^{-1} for velocity and 1/2 m.s^{-2} for acceleration. As detailed in Appendix D, a Barzilai Borwein gradient approach is then applied to get more precise results. It converges relatively fast. For instance, Fig. 6 has been obtained with an average number of 20 iterations in gradient ascent per trial.

The performance curves exhibit the three typical regions observed in non-linear estimation [38], [39]: the no information region driven by ambiguity errors at very low E_b/N_0, the threshold region that characterizes the transition from global to local errors and the asymptotic region at high E_b/N_0 driven by mainlobe errors. CSB and MBA show very similar performance, with a slight gain for CSB. Both estimators are limited by an error floor mainly due to the very rich multipath environment and the residual Doppler scaling differences between taps. MBA is also affected by the use of a finite step for the grid-search optimization. The main conclusion here is that the cyclostationary features of communication signals can provide accurate estimates of the Doppler scale without pilot overhead. In addition, both methods can be implemented using FFTs and have therefore order of $\mathcal{O}\left(N_{\text{obs}} \log(N_{\text{obs}})\right)$ complexity, where N_{obs} is the number of signal samples over the duration T_{obs}. However, the actual complexity depends on constant factors that may be slightly different between the two methods. For instance, in this specific example, MBA is twice more complex than CSB because the grid step used for the cost function optimization is smaller than the one used in our method. In addition, as discussed in [31, Sec. III-B], if higher accelerations were to be considered, MBA would require signal resampling that would result in a significant complexity burden. This is not the case for CSB as its complexity increases linearly with a_m.

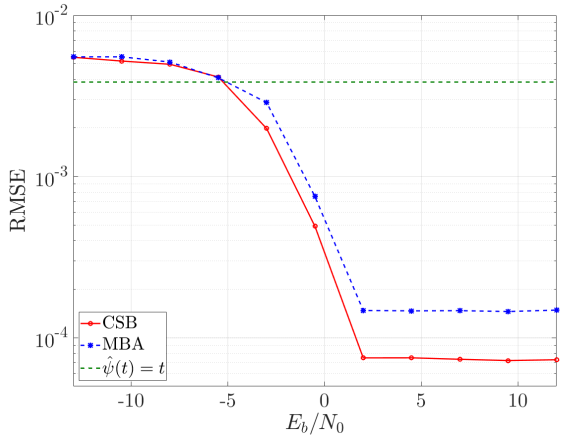

Fig. 6: Performance comparison between the multibranch autocorrelation (MBA) estimator and the cyclostationary-based (CSB) method.

2) MSML channel : The previous estimator can be extended to the general model (6) with multiple Doppler scales. More specifically, for $u = 0$ and for PSK/QAM signals in MSML channels, Eq. (16) simplifies to

$$R_{y_\ell,y_m}(t,0) = e^{i2\pi f_c\left(\tau_\ell-\tau_m+\left(\frac{v_\ell-v_m}{c}\right)t+\left(\frac{a_\ell-a_m}{2c}\right)t^2\right)} \times \sum_{n=-1}^{1} R_x^{\frac{n}{T_s}}(\tau_\ell-\tau_m)e^{i2\pi\frac{n}{T_s}(\psi_\ell(t)-\tau_\ell)}. \tag{25}$$

As illustrated in Fig. 1-(a), $R_x^{\frac{n}{T_s}}(u)$ quickly decreases with u. For instance, for RRC filters and for $n \neq 0$, the width of the mainlobe of $R_x^{\frac{\pm 1}{T_s}}(u)$ is $3T_s/\xi$. Hence, we can reasonably assume that $R_x^{\frac{n}{T_s}}(\tau_\ell-\tau_m) \approx 0$, if $|\tau_\ell-\tau_m| > \frac{3T_s}{2\xi}$ so that $R_{y_\ell,y_m}(t,0) \approx 0$ in this case. This means that if the multipath arrivals are too delayed with each other, then they are no longer jointly cyclostationary. In addition, for small differences in delay, i.e. $|\tau_\ell-\tau_m| \leq \frac{3T_s}{2\xi}$, we make the approximation that $v_\ell \approx v_m$ and $a_\ell \approx a_m$. Such an approximation is a way of stating that paths with significantly different Doppler scales should be resolved within the signal bandwidth. If not, interfering terms depending on the velocity and acceleration differences appear in the autocorrelation function and make it difficult to differentiate the contribution of each time-warping function. Based on this analysis, for any ℓ and m, Eq. (25) can be simplified to

$$R_{y_\ell,y_m}(t,0) = e^{i2\pi f_c(\tau_\ell-\tau_m)} \times \sum_{n=-1}^{1} R_x^{\frac{n}{T_s}}(\tau_\ell-\tau_m)e^{i2\pi\frac{n}{T_s}(\psi_\ell(t)-\tau_\ell)}. \tag{26}$$

Therefore, similarly to Eq. (20), the zero-lag autocorrelation function of the received signal can be expressed as

$$R_r(t,0) = \sum_{\ell=1}^{L} 2\Re\left\{A_\ell e^{i\frac{2\pi}{T_s}\psi_\ell(t)}\right\} + K, \tag{27}$$

with $A_\ell \in \mathbb{C}$ and $K \in \mathbb{R}$. Because of the transmission geometry, it is very common in practice that several taps share (nearly) the same time-warping function ψ_ℓ. Let $\mathcal{L}_d$ denote the set of tap indexes with the same function ψ_d. Assuming that the channel contains $D \leq L$ different Doppler scales, a more practical formulation of (27) may then be

$$R_r(t,0) = \sum_{d=1}^{D} 2\Re\left\{\Gamma_d e^{i\frac{2\pi}{T_s}\psi_d(t)}\right\} + K, \tag{28}$$

where $\Gamma_d = \sum_{\ell\in\mathcal{L}_d} A_\ell$.

The proposed estimation procedure relies on (28). It is iterative and very much like a matching-pursuit procedure. At each iteration j, the dominant Doppler scale is estimated using (22). Then, the contribution of the dominant "Doppler chirp" in (28) is subtracted after estimating its amplitude $\Gamma^{(j)}$. The procedure is repeated until a stopping criterion is reached. Similarly to the approach described in Sec. III-C1, we cannot observe $R_r(t,0) = \mathbb{E}\{|r(t)|^2\}$ so we rely on its estimate $\hat{R}_r(t,0) = |r(t)|^2$. The full method is detailed in Alg. 1. There can be several ways of stopping the iterative procedure. It can be stopped once a given number D_{max} of significant Doppler scales is reached. This number could be (roughly) known a priori based on the knowledge of the transmission geometry. Another approach could be to stop the procedure once the combined amplitudes of the paths with the same Doppler scale is considered to be too small to be of interest, i.e., when $|\widehat{\Gamma}^{(j)}|/|\widehat{\Gamma}^{(0)}| < \epsilon$ in Alg. 1. The iterative procedure is illustrated in Fig. 7 through the evolution of the cost function $J_{r^{(j)}}$ in a channel with two Doppler scales. At iteration $j = 0$, we observe two local maxima revealing the presence of two Doppler scales. The strongest scale is estimated and then subtracted from the observation $|r^{(j+1)}(t)|^2$. At iteration $j = 1$, the cost function shows only one maximum corresponding to the single remaining Doppler scale.

To further illustrate the performance of CSB, we consider a deep-water multiscale-multilag channel with a *Munk* sound speed profile [32]. All the simulation parameters are identical to those described in the previous section, except that the water and RX depths are set to 5000 and 200 m, respectively. The initial TX depth is 25 m, the TX/RX range is set to 200 m and the transmitter moves towards the surface. Such a configuration is known to be difficult for

Algorithm 1 Multiscale Doppler estimation

Input: $r(t)$, D_{max}

$j = 0$

$r^{(j)}(t) = r(t)$

stop=false

while stop=false **do**

$\left(\widehat{\mu}_1^{(j)}, \widehat{\mu}_2^{(j)}\right) = \text{argmax}_{(\mu_1,\mu_2)}\, J_{r^{(j)}}(\mu_1, \mu_2)$

$\widehat{\psi}^{(j)}(t) = \widehat{\mu}_1^{(j)} t + \widehat{\mu}_2^{(j)} t^2$

$\widehat{\Gamma}^{(j)} = \frac{1}{T_{\text{obs}}} \int_0^{T_{\text{obs}}} |r(t)|^2 e^{-i\frac{2\pi}{T_s}\widehat{\psi}^{(j)}(t)} \mathrm{d}t$

$|r^{(j+1)}(t)|^2 = |r^{(j)}(t)|^2 - 2\Re\left\{\widehat{\Gamma}^{(j)} e^{i\frac{2\pi}{T_s}\widehat{\psi}^{(j)}(t)}\right\}$

stop=compute_stopping_criterion $\left(n, D_{\text{max}}, \widehat{\Gamma}^{(j)}\right)$

$j = j + 1$

end while

Output: $\{\widehat{\psi}^{(j)}(t)\}_{j=0}^{D_{\text{max}}-1}$

communications systems as the time-varying channel is mostly made of two paths with similar amplitudes and opposite-sign Doppler scales. For multiscale channels, the performance metric is now defined as:

$$\text{RMSE}_{\text{ms}} = \sqrt{\frac{\sum_{d=1}^{D_{\text{max}}} |\Gamma_d| \times \mathbb{E}\left\{\int_0^{T_{obs}} \left(\widehat{\psi}_d(t) - \psi_d(t)\right)^2 \mathrm{d}t\right\}}{\sum_{d=1}^{D_{\text{max}}} |\Gamma_d| \times \mathbb{E}\left\{\int_0^{T_{obs}} \psi_d^2(t) \mathrm{d}t\right\}}}, \tag{29}$$

where $D_{\text{max}} = 2$ in this specific scenario.

The MBA curve in Fig. 8 shows that using a single Doppler scale estimator in a multiscale environment can be worse than not performing any estimation at all (i.e, $\widehat{\phi}(t) = t$). The figure also shows that CSB can be highly efficient in multiscale channels. In our scenario, the asymptotic regime is reached for a value of E_b/N_0 as low as 0 dB. Detecting and estimating multiple Doppler scales can be useful to trigger post-processing to make the communication link more robust. For instance, it can be used to optimize the choice of the equalizer or PLL parameters. It can also trigger a change of waveform if the transmitter is adaptive, or some array-processing to separate multipath signals with different scales.

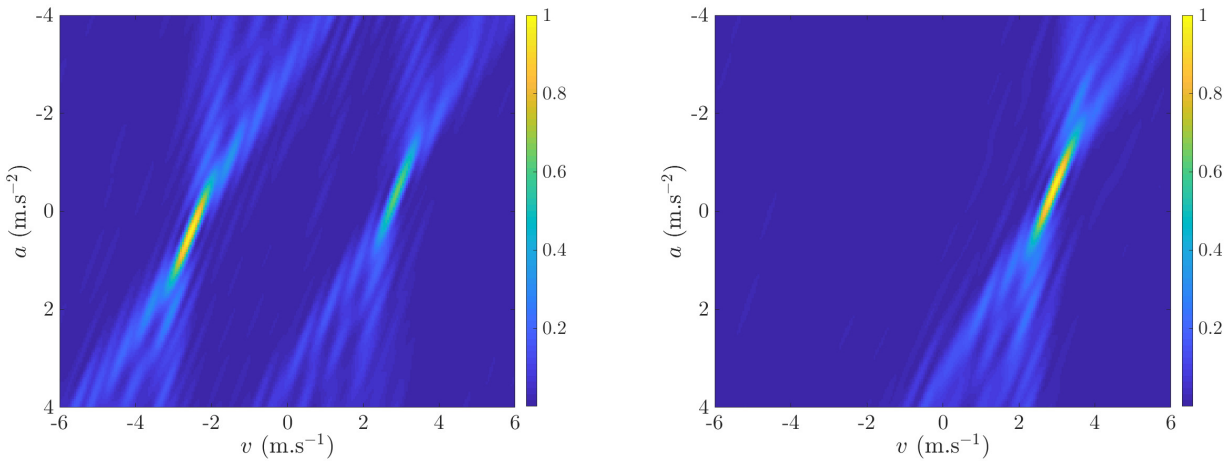

Fig. 7: Example of the evolution of the cost function $J_{r^{(j)}}$ obtained in a MSML channel simulated with Bellhop. (a) Iteration $j = 0$, (b) iteration $j = 1$. The cost is expressed as a function of velocity and acceleration based on model (8) with $c = 1500$ m.s^{-1}, i.e., $v = 1500(1 - \mu_1)$ and $a = -3000\mu_2$. $T_{obs} = 1$ s, $T_s = 0.2$ ms, $f_c = 20$ kHz, $E_b/N_0 = 5$ dB.

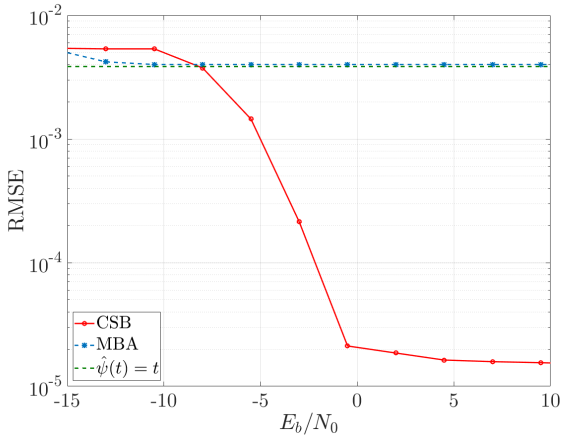

Fig. 8: Performance of the cyclostationary-based (CSB) method in a multiscale-multilag channel.

3) Extension to other modulations: The proposed Doppler scale estimator can be extended to any second-order CS signal. The key is to consider a cost function J_r that makes use of the specific CS features of the signal of interest. For instance, based on the analysis of Appendix A-C, we can sum the cost function (23) over several cycle frequencies rather than just one to

make it relevant for DSSS signals. By considering non zero-lag correlations, this cost can also be adapted to OFDM signals. All of this is related to the concept of cyclostationary signatures that is formally defined in the next paragraph. A general formulation of the cost function applicable to any kind of CS features is proposed in Eq. (35). Although used for detection purposes in the next paragraph, this cost also provides a Doppler scale estimation.

D. Application 2: signal detection in impulsive noise

As a second application, we consider the problem of detecting an underwater acoustic signal with a specific cyclostationary signature. We define a signature of a signal $x(t)$ as a subset $\mathcal{S} \subseteq \mathcal{C}$, where $\mathcal{C} = \{(u,\alpha) :\ R_x^\alpha(u) \neq 0\}$. Such a signature may be unique and therefore relevant to detect/identify a specific communication system in underwater warfare-like applications. Based on the observation $r(t)$ and the knowledge of $\mathcal{S}$, the detection problem addressed in this section is to decide between the following hypotheses

$$\begin{cases} \mathcal{H}_0 :\ \ R_x^\alpha(u) = 0,\ \forall\,(u,\alpha) \in \mathcal{S} \\ \mathcal{H}_1 :\ \ R_x^\alpha(u) \neq 0,\ \forall\,(u,\alpha) \in \mathcal{S}. \end{cases} \tag{30}$$

Without loss of generality, we take OFDM signals with subcarrier-spacing Δ_f, guard-time T_g and symbol duration T_s as examples. As illustrated in Fig. 1 and Appendix A-B, possible signatures are $\mathcal{S} = \left\{\left(0, \frac{n}{T_s}\right), n = -N_\alpha, \cdots, N_\alpha\right\}$ for ZP-OFDM, $\mathcal{S} = \left\{\left(\frac{1}{\Delta_f}, \frac{n}{T_s}\right), n = -N_\alpha, \cdots, N_\alpha\right\}$ for CP-OFDM and $\mathcal{S} = \{(nT_s, 0), n = -N_u, \cdots, N_u\}$ for SIP-OFDM, with N_α and N_u the number of cycle frequencies and delays of interest, respectively.

Problem (30) has already been addressed in the context of terrestrial radio-communications and existing solutions rely on the computation of the following test statistic (or variations of it) [40]–[44]

$$J_r^{\text{CS}} = \frac{1}{T_{\text{obs}}} \sum_{(u,\alpha)\in\mathcal{S}} \left| \int_0^{T_{\text{obs}}} r^*(t) r(t+u) e^{-i2\pi\alpha t} \mathrm{d}t \right|^2. \tag{31}$$

It can be interpreted as the power estimate of the cyclic autocorrelation function on support $\mathcal{S}$. To adapt it to the underwater context, we must take into account the motion-induced compression or dilation of the signal. A brute-force approach is to rely on Eq. (14) and de-warp $r(t)$ prior to the computation of (31). Since the dominant warping function is not known a priori, this

involves an optimization over several candidate functions and a new test statistic can be

$$J_r^{\text{DCS}} = \max_{(\mu_1,\mu_2)} \frac{1}{T_{\text{obs}}} \sum_{(u,\alpha)\in\mathcal{S}} \left| \int_0^{T_{\text{obs}}} \hat{\rho}_{\mu_1,\mu_2}\left(\psi^{-1}_{\mu_1,\mu_2}(t), \psi^{-1}_{\mu_1,\mu_2}(t+u)\right) e^{-i2\pi\alpha t} \mathrm{d}t \right|^2, \tag{32}$$

where

$$\hat{\rho}_{\mu_1,\mu_2}(t, t+u) = r^*(t) r(t+u) e^{-i2\pi f_c\left(\psi_{\mu_1,\mu_2}(t+u) - \psi_{\mu_1,\mu_2}(t) - u\right)}, \tag{33}$$

with

$$\psi_{\mu_1,\mu_2}(t) = \mu_1 t + \mu_2 t^2, \quad \psi^{-1}_{\mu_1,\mu_2}(t) = \begin{cases} \frac{1}{2\mu_2}\left(\sqrt{\mu_1^2 + 4\mu_2 t} - \mu_1\right), & \mu_2 \neq 0, \\ \frac{t}{\mu_1}, & \mu_2 = 0,\ \mu_1 \neq 0 \end{cases} \tag{34}$$

In practice, the implementation of de-warping in (32) requires to resample the discrete-time version of $r(t)$ for each candidate pair (μ_1, μ_2), which is computationally costly. A less complex approach is to rely on approximation (13) so that the previous test statistic can be approximated as

$$J_r^{\text{ADCS}} = \max_{(\mu_1,\mu_2)} \frac{1}{T_{\text{obs}}} \sum_{(u,\alpha)\in\mathcal{S}} \left| \int_0^{T_{\text{obs}}} r^*(t) r\left(t + \psi^{-1}_{\mu_1,\mu_2}(u)\right) e^{-i2\pi\left(\alpha\psi_{\mu_1,\mu_2}(t) + 2\mu_2 u f_c t\right)} \mathrm{d}t \right|^2. \tag{35}$$

As discussed in Appendix E, the computation of this statistic does not involve any resampling.

To further adapt our approach to the underwater context, the additive noise is assumed to be possibly impulsive or transient [45]–[48]. This type of noise can be generated by man-made activities, biological or geophysical sources and is sometimes caused by faulty elements in the receiver front-end. In heavy-tailed noise or when the noise statistics are not fully known, a non-linear function is usually applied to the observed signal $r(t)$ before further processing. It provides robustness and reduces the influence of outliers [42], [49]. A simple and efficient example is the spatial-sign function defined as [50]

$$\mathrm{s}(r(t)) = \begin{cases} \frac{r(t)}{|r(t)|} & \text{if } r(t) \neq 0 \\ 0 & \text{otherwise.} \end{cases} \tag{36}$$

For $u \neq 0$, spatial-sign cyclic correlation estimators are then obtained by replacing $r(t)$ with $\mathrm{s}(r(t))$ in Eqs (31)-(35).

Based on this analysis, we define three robust cyclostationary-based detectors:

- the cyclostationary (CS) detector: $J^{\text{CS}}_{\mathrm{s}(r)} \underset{H_0}{\overset{H_1}{\gtrless}} \Lambda^{\text{CS}}$,
- the de-warped cyclostationary (DCS) detector: $J^{\text{DCS}}_{\mathrm{s}(r)} \underset{H_0}{\overset{H_1}{\gtrless}} \Lambda^{\text{DCS}}$,

- the approximated de-warped cyclostationary (ADCS) detector: $J_{\mathrm{s}(r)}^{\mathrm{ADCS}} \underset{H_0}{\overset{H_1}{\gtrless}} \Lambda^{\mathrm{ADCS}}$,

where Λ^{CS}, Λ^{DCS} and Λ^{ADCS} are detection thresholds set to achieve a given false-alarm probability P_{FA}. Note that these detectors are scale-invariant thanks to the spatial-sign function. Moreover, as opposed to the estimator described in Alg. 1, these detectors focus on the most powerful tap and do not track secondary taps. This is a common behavior for detectors since the actual delay-Doppler parameters of taps with low amplitudes are very unlikely to be correctly estimated for low SNRs and may result in noise injection in the test statistics [51]. Finally, DCS and ADCS also offer the advantage of providing an estimate of the relative velocity and acceleration through the maximization over (μ_1, μ_2). This additional information can be useful for other applications such as source tracking or identification.

The performance of these detectors is illustrated with real CP-OFDM data [20] collected in shallow water (20-60 m deep) off the coast of Brest, France, in June 2017. Transmissions were carried out to a 5-element receiving array at distances ranging from 20 m to 3 km. Both the source and the array were immersed from drifting ships and the source was mounted on a rigid pole. The sea state was rough with a 4 m swell. Experiments were conducted in two bandwidths: $[8 - 19.75]$ kHz and $[20.25 - 32]$ kHz. The OFDM parameters were kept constant and set as given in Table I.

TABLE I: OFDM parameters

Filter	Constellation	Δ_f (Hz)	T_g (ms)	T_s (ms)	Num. of subcarriers
RRC - $\xi = 1/3$	QPSK	16.7	20	80	705

Fig. 9 shows spectrogram examples of received OFDM packets under various noise and propagation conditions. Each packet is 2 s long followed by 1 s of silence and the dataset is made of 775 packets in each bandwidth. The detectors are tested with T_{obs} set to 0.5 s so that the total number of signals per bandwidth is 3100. Each hydrophone is processed individually without any array processing. Fig. 10 shows the SNR distribution of the dataset in each bandwidth. SNR was estimated by combining power measurements of noise-only and signal-plus-noise portions of the observation.

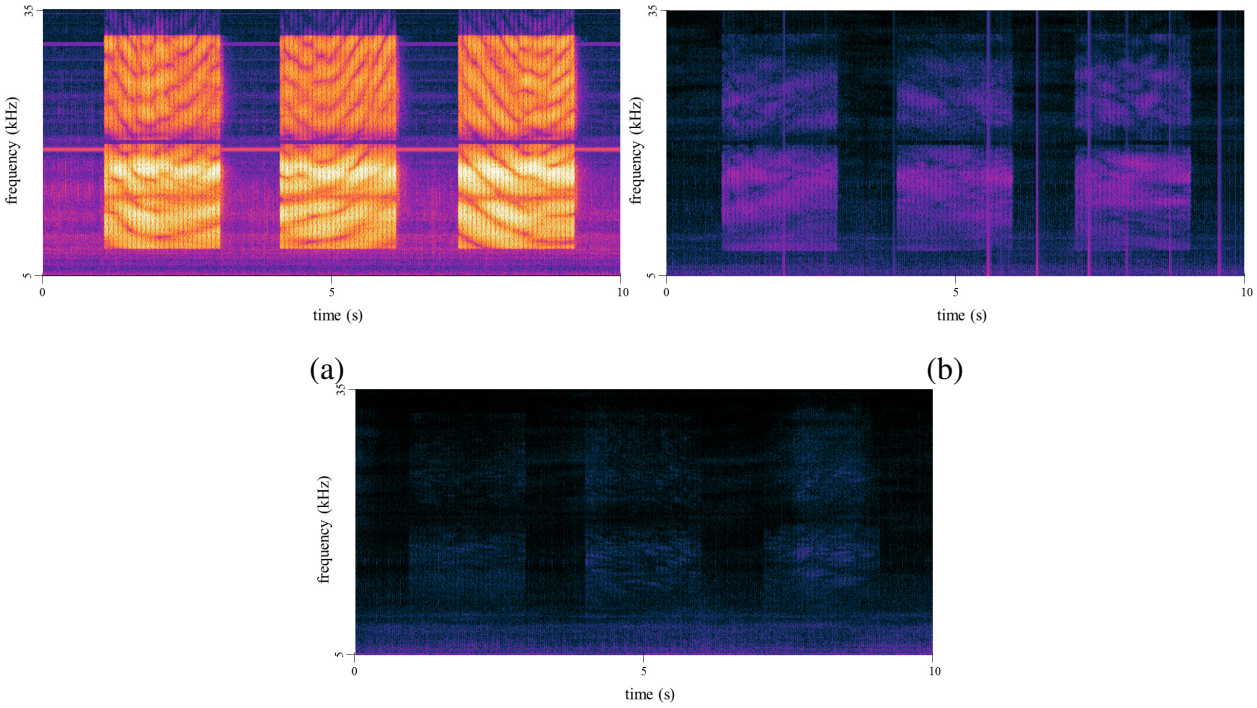

Fig. 9: Spectrogram examples of received OFDM packets. (a) High SNR packets with tonal noise, (b) moderate SNR packets with impulsive noise, (c) low SNR packets.

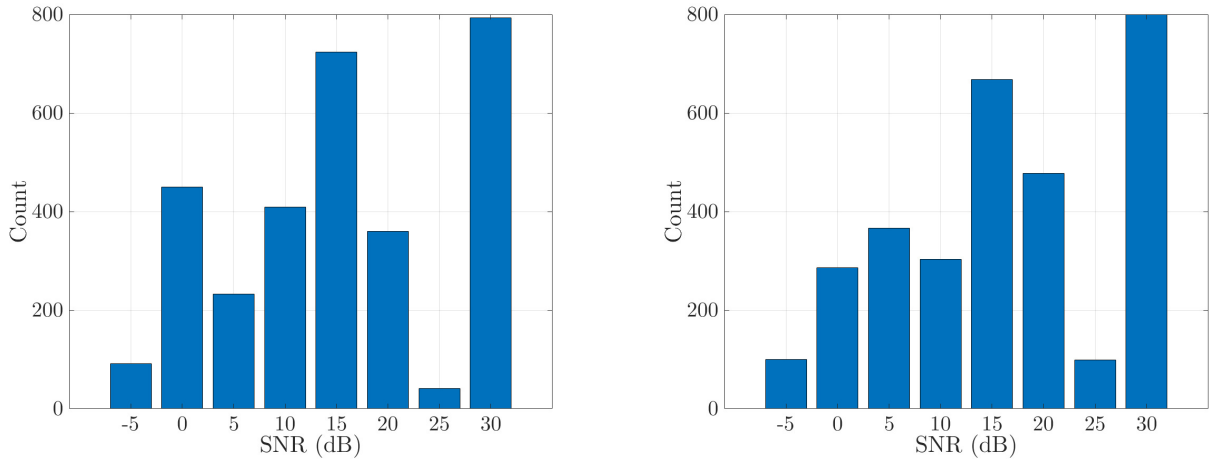

Fig. 10: SNR distribution of the OFDM dataset, (a) $[8 - 19.75]$ kHz, (b) $[20.25 - 32]$ kHz.

The signature of the OFDM signal is defined as $\mathcal{S} = \left\{ \left(\frac{1}{\Delta_f}, \frac{n}{T_s} \right), 0 < |n| \leq 3 \right\}$. The cycle frequency $\alpha = 0$ is not considered because tonal noise may imply that $R_w^0 \left(\frac{1}{\Delta_f} \right) \neq 0$, which would result in false alarms. Moreover, to limit complexity without significant performance penalty, no cycle frequency higher than $3/T_s$ is considered in the signature. For the DCS and ADCS detectors, the maximization over (μ_1, μ_2) is restricted to the interval $[1 - 1/3.10^{-2}, 1 + 1/3.10^{-2}] \times [-10^{-3}, 10^{-3}]$. With a sound speed of 1500 m.s^{-1}, this corresponds to a maximum velocity of 5 m.s^{-1} and a maximum acceleration of 3 m.s^{-2}. The latter value may seem large but strong accelerations were observed due to the rough sea condition combined with the fact that the source was mounted on a rigid pole. This is illustrated in Fig. 11 where two examples of the cost function in Eq. (32) are displayed as a function of velocity and acceleration using model (8). Both the single and multiscale examples exhibit acceleration of several meters per second squared.

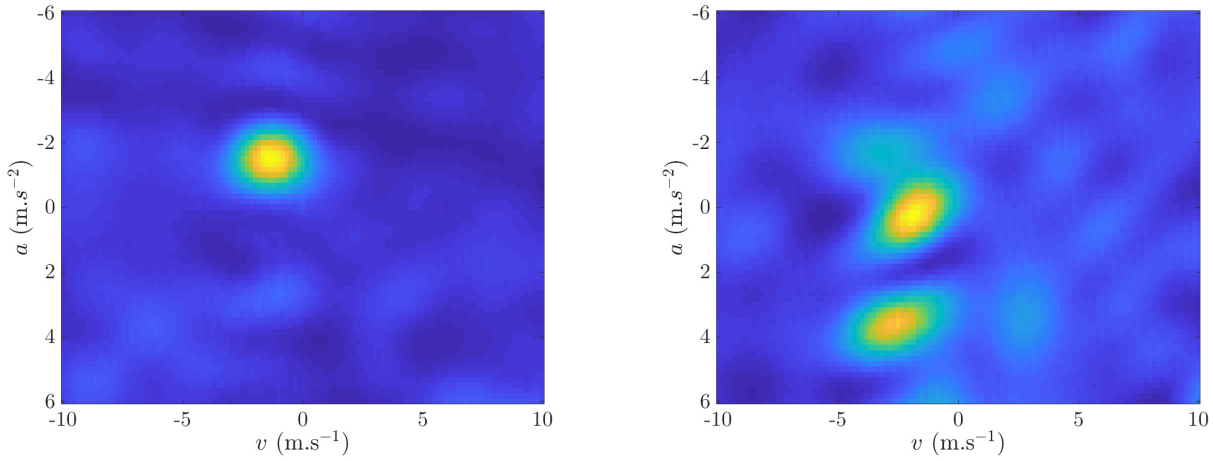

(a) (b)

Fig. 11: Examples of the cost to maximize in Eq. (32) as a function of velocity and acceleration, bandwidth: $[20.25 - 32]$ kHz, distance: few tenths of meters. (a) Single scale multilag channel, (b) multiscale-multilag channel.

The performance of the proposed detectors is investigated in terms of detection rate. The detection thresholds are obtained with Monte-Carlo trials on real underwater noise and set such that the false alarm rate equals 10^{-6}. For both the DCS and ADCS detectors, the maximization

is performed using a grid search approach with a step set to $1/3.10^{-3}$ for μ_1 and to $1/6.10^{-3}$ for μ_2. Fig. 12 shows the detection rate as function of SNR for the two bandwidths. It clearly highlights the benefit of explicitly considering the specificity of the underwater channel. For both channels, CS performs poorly. This is expected since the possible compression or dilation of the signal is not taken into account. Fig. 12 also supports the use of ADCS. This detector provides very similar performance to DCS while being computationally less expensive. Finally, performance in the $[20.25 - 32]$ kHz bandwidth is not as good as for lower frequencies. Even for SNRs above 15 dB, the detection rate does not reach 100%. Analysis of the test statistics shows a greater number of multiscale Doppler occurrences in the higher frequency band. This is especially true for transmission range less than 1 km and thus for high SNRs. As illustrated in Figure 11, multiscale Doppler splits the power of the cost function between two (or more) local maxima and thus reduces the probability of detection. Without channel sounding data, it is difficult to conjecture a physical interpretation of these results. We can only say that they are attributable to frequency dependent phenomena.

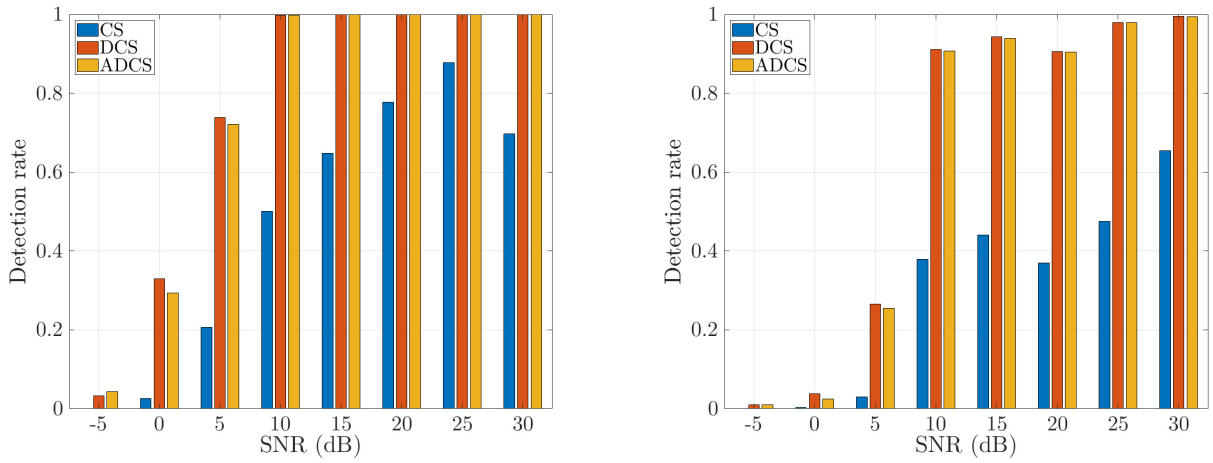

(a) (b)

Fig. 12: Detection rate of OFDM signals as a function of SNR. (a) $[8-19.75]$ kHz, (b) $[20.25-32]$ kHz.

IV. Cyclostationarity in dispersive channels

A. Channel model

The previous MSML model is not applicable to all communication scenarios, especially at (very) low-frequency. Propagation in such a scenario is better described by normal-mode theory. Considering a broadband source emitting at depth z_s in a range-independent waveguide, the baseband spectral component of the pressure field $R(\nu)$ received at depth z_r after propagation over a range r_s is given by

$$R(\nu) = H(\nu)X(\nu) + W(\nu), \tag{37}$$

where $X(\nu)$ and $W(\nu)$ are the baseband source and noise spectrum, respectively. $H(\nu)$ denotes the deterministic channel transfer function expressed as [11, Ch. 5]

$$H(\nu) = \sum_{m=1}^{M} A_m\left(\nu + f_c\right) e^{i\theta_m(\nu+f_c)}, \tag{38}$$

where M is the number of propagating modes, f_c is the carrier frequency and

$$A_m\left(\nu\right) = \frac{Q}{\sqrt{k_{rm}(\nu)r_s}}\psi_m(\nu, z_s)\psi_m(\nu, z_r) \tag{39}$$

and

$$\theta_m\left(\nu\right) = r_s k_{rm}(\nu). \tag{40}$$

k_{rm} and ψ_m are the horizontal wavenumber and modal depth function of mode m, respectively. The quantity $Q = \frac{e^{j\pi/4}}{\sqrt{8\pi}\rho(z_s)}$ represents a constant factor with $\rho(z_s)$ as the water density at the source depth z_s. For notational convenience, the dependencies in r_s, z_s and z_r are dropped for $H(\nu)$. The modal amplitude mostly depends on source/receiver depth and weakly on range, whereas the modal phase primarily depends on range.

Channel (38) is said to be dispersive because, for each mode, different frequencies are time-shifted by different amounts. For mode m, the modal travel time is [52, Eq. (4)]

$$t_m(\nu) = \frac{1}{2\pi}\frac{\partial\theta_m\left(\nu\right)}{\partial\nu} = \frac{r_s}{v_m(\nu)}, \tag{41}$$

where $v_m(\nu) = \partial\nu/\partial k_{rm}(\nu)$ denotes the modal group speed. Such a channel exhibits intermodal dispersion (each mode has its own travel time) as well as intramodal dispersion (for a given mode, the travel time is frequency dependent). Fig. 13 illustrates these phenomena in a Pekeris

waveguide for a water depth of 50 m and two ranges.[3] This figure shows the channel power delay profiles in the upper panels (a) and (b) and the spectrogram of the impulse responses in the bottom ones, (c) and (d). There are four propagating modes and modal dispersion is clearly visible on the spectrograms, especially for $r_s = 25$ km. Each mode is distinguishable and the frequency dependency of the travel time is manifest. This figure also shows that modal dispersion increases with range which makes the channel delay-spread increase as well. In addition, no dominant taps are visible and the power-delay profiles are not sparse. Finally, in this kind of channel, each mode acts as a high-pass filter. Below a given mode-dependent cut-off frequency, no propagating energy is excited in the water column and the acoustic field leaks into the bottom [11]. For instance, in the simulated channel, the cut-off frequencies ν_{cm} of each mode are: $\nu_{c1} \approx 21.5$ Hz, $\nu_{c2} \approx 64.6$ Hz, $\nu_{c3} \approx 107.7$ Hz and $\nu_{c4} \approx 150.9$ Hz. Therefore, when these cut-off frequencies are inside the chosen frequency band, dispersive channels can be highly frequency-selective.

B. Cyclostationary analysis

Since the dispersive channel (38) acts as a time-invariant linear system, if the input signal $x(t)$ is cyclostationary, periodicity in the time-varying correlation at the output is still expected. More specifically, it can be shown that the cyclic autocorrelation function of $r(t)$ satisfies [2, Eq. (3.83)]

$$R_r^\alpha(u) = R_x^\alpha(u) \circledast_u \int h^*(t)h(t+u)e^{-i2\pi\alpha t}\mathrm{d}t + R_w(u), \tag{42}$$

where $h(t)$ is the channel impulse response and $\circledast_u$ denotes convolution with respect to u. The cyclic spectrum is therefore expressed as [2, Eq. (3.84)]

$$S_r^\alpha(\nu) = S_x^\alpha(\nu)H^*\left(\nu-\alpha\right)H(\nu) + S_w^0(\nu), \tag{43}$$

where $S_w^0(\cdot)$ is the noise power spectral density. Although the last two equations indicate that the cyclostationary features are preserved at reception, this has to be balanced by the actual physical properties of the channel. As mentioned previously, each mode has a cut-off frequency and this high-pass behavior may prevent or limit the propagation of some cycle frequencies. More precisely, based on (38), we have

$$H^*\left(\nu-\alpha\right)H(\nu) = \sum_{m=1}^{M}\sum_{n=1}^{M} A_m^*\left(\nu+f_c-\alpha\right)A_n\left(\nu+f_c\right)e^{i(\theta_n(\nu+f_c)-\theta_m(\nu+f_c-\alpha))}. \tag{44}$$

[3]A Pekeris waveguide consists in an isospeed water layer overlaying a semi-infinite fluid basement [53].

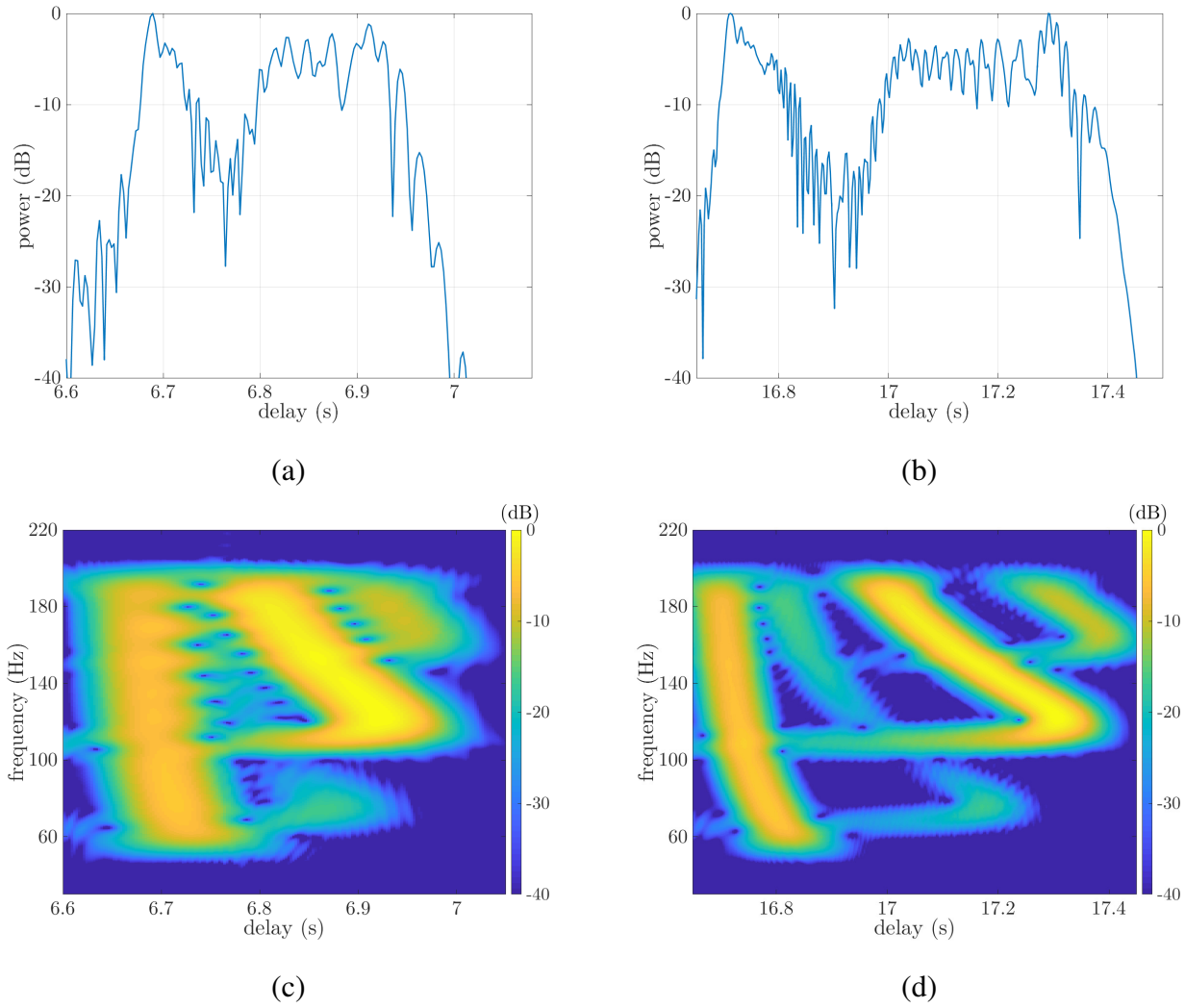

Fig. 13: Simulated channels in a Pekeris waveguide, frequency range: $[60-190]$ Hz, water depth: 50 m, $z_s = 10$ m, $z_r = 30$ m, sound speed in seawater 1500 m.s^{-1}, density 1000 kg.m^{-3}, sound speed in the bottom 1600 m.s^{-1} and density 1800 kg.m^{-3}. Left column: $r_s = 10$ km, right column: $r_s = 25$ km. First row: channel power delay profiles, second row: spectrograms of the impulse responses.

If B denotes the monolateral bandwidth of transmission and ν_{cm} the cut-off frequency of mode m, then

$$A_m^* \left(\nu + f_c - \alpha\right) A_n \left(\nu + f_c\right) = 0 \tag{45}$$

for any $\alpha \in (-\infty, \max(-2B, -(B + f_c - \nu_{cn}))] \cup [\min(2B, B + f_c - \nu_{cm}), +\infty)$. Therefore, a given mode m will not propagate cycle frequencies greater than $\alpha_{cm} \triangleq \min(2B, B + f_c - \nu_{cm})$. For instance, in the Pekeris waveguide of Fig. 13, modes 1 and 3 are the most energetic with $\nu_{c1} \approx 21.5$ Hz and $\nu_{c3} \approx 107.7$ Hz. Since $f_c = 125$ Hz and $B = 65$ Hz, mode 1 will propagate all the cycle frequencies within the transmission bandwidth, that is $\alpha_{c1} = 2B = 130$ Hz. However, for mode 3, we have $\alpha_{c3} = 82.3$ Hz so that cycle frequencies $|\alpha| > \alpha_{c3}$ will not be propagated by this mode. This analysis is illustrated in Fig. 14 where the power spectral density $|H(\nu)|^2$ is shown for $r_s = 25$ km as well as the product $|H^*(\nu - \alpha) H(\nu)|$. The left graph shows the effect of the cut-off frequency ν_{c3} on the channel selectivity. Stronger attenuation are observed on the power spectral density for $\nu < \nu_{c3} - f_c$. The graph on the right shows that this cut-off frequency also impacts the attenuation of cycle frequencies. As expected, cycle frequencies outside the range $[-\alpha_{c3}, \alpha_{c3}]$ will be more affected by the channel.

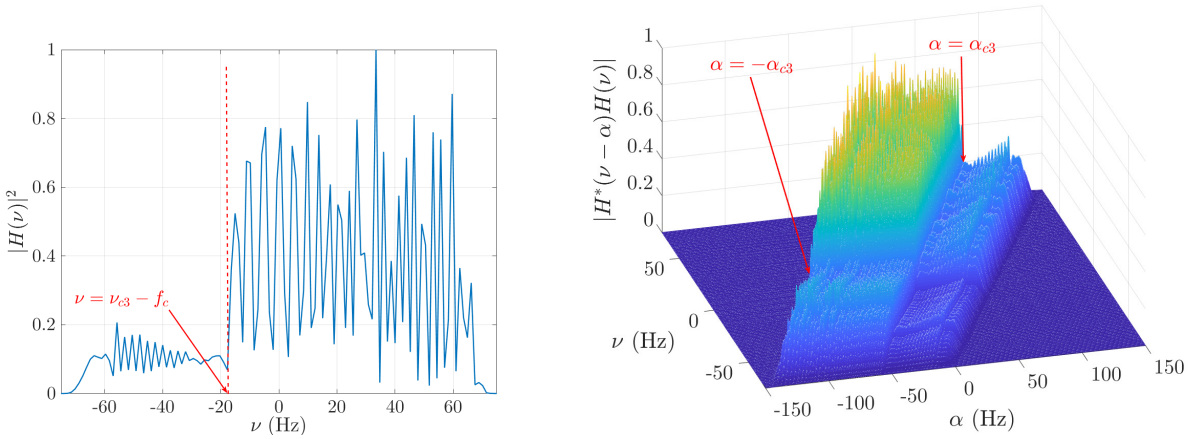

(a) (b)

Fig. 14: Effect of the mode cut-off frequency on the channel selectivity and on the cycle frequencies. Illustration with the Pekeris waveguide of Fig. 13, $r_s = 25$ km. (a) Channel power spectral density, (b) product $|H^*(\nu - \alpha) H(\nu)|$.

Moreover, it is also worth mentioning that modal dispersion will affect the shape of the cyclic autocorrelation function. This is illustrated in Fig. 15 where this function is plotted for a DSSS signal at the input and output (without noise) of a dispersive channel. The cycle frequency is set to $\alpha = 1/T_s$. It can be seen that the frequency dependency of travel time t_m in Eq. (41) shifts

and spreads the cyclic autocorrelation function along the lag-axis u. Although the signal remains cyclostationary at the channel output, care must therefore be taken when designing estimators or detectors. For instance, the CS signature detector presented in Sec. III-D would perform poorly in an unknown dispersive channel.

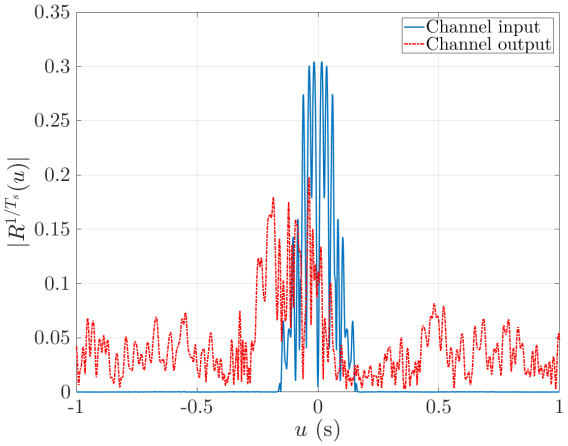

Fig. 15: Effect of the modal dispersion on the cyclic autocorrelation function of the DSSS signal of Sec. IV-C, $\alpha = 1/T_s$. The channel is the Pekeris waveguide of Fig. 13, $r_s = 25$ km.

In summary, unlike MSML channels, this short analysis shows that it is not necessary to modify the standard statistical framework to recover the cyclostationary features at the output of a dispersive channel. This means that the existing tools [2] designed to detect, estimate, filter, etc. cyclostationary signals can be used in this kind of environment with little adaptation. However, one should be aware that dispersive channels may attenuate the higher cycle frequencies and may also shift and spread the amplitude of the cyclic autocorrelation function along the time-lag axis.

C. Application

To illustrate the previous analysis, we consider the problem of eavesdropping on a low-frequency covert communication. More specifically, we assume that the transmitter uses a DSSS waveform, as in Eq. (74), to limit the probability of being detected and reverse-engineered. We take the viewpoint of the eavesdropper and seek to blindly estimate the symbol duration T_s of the transmitted signal. We also consider that the eavesdropper may have an array with several

hydrophones to intercept the signal. No assumptions about the spreading sequence and the chip rate are made.

As shown in Appendix A-C, DSSS signals are cyclostationary with period T_s. Therefore, estimating the symbol duration amounts to estimating the fundamental period of $R_x(t,u)$ from the received signals. In short, our problem is a joint cycle-frequency detection and estimation problem. Similar problems have already been addressed in the literature and a simple yet efficient statistic to detect unknown cycle frequencies is the estimate of the spectral coherence density (SCD) defined as [54]

$$C_r^{\alpha}(\nu) \triangleq \frac{S_r^{\alpha}(\nu)}{\sqrt{S_r^0(\nu)S_r^0(\nu-\alpha)}}. \tag{46}$$

A key feature of the SCD is that it is normalized and therefore scale-invariant. It also equalizes regions with different energy levels and can thus reveals weak cycle frequencies. Based on the observation of a finite duration signal $r(t)$, the SCD can be estimated using cyclic spectrum estimators such as the FFT accumulation method (FAM), the strip spectral correlation analyzer (SSCA) [55], cyclic periodograms [56] or the fast method described in [57]. To adapt this approach to our SIMO context and make an optimal use of the array at reception, we propose to compute the SCD at the output of each hydrophone but also between hydrophones. In fact, the channel model of Eq. (38) implies that the received signals along the array will remain correlated. Therefore, we define the set of estimated cycle frequencies as

$$\hat{\mathcal{A}} = \left\{ \alpha : \max_{\nu} \left| \sum_{n=1}^{N_h} \sum_{m=n}^{N_h} \hat{C}_{r_n,r_m}^{\alpha}(\nu) \right| > \Lambda^{\mathrm{DC}} \right\}, \tag{47}$$

where N_h denotes the number of hydrophones, r_n is the received signal on the n-th hydrophone, Λ^{DC} is a detection threshold and $\hat{C}_{r_n,r_m}^{\alpha}$ is an estimate of the spectral cross-coherence density defined as

$$C_{r_n,r_m}^{\alpha}(\nu) \triangleq \frac{S_{r_n,r_m}^{\alpha}(\nu)}{\sqrt{S_{r_n,r_m}^0(\nu)S_{r_n,r_m}^0(\nu-\alpha)}}, \tag{48}$$

where $S_{r_n,r_m}^{\alpha}(\nu)$ is the cyclic cross-spectrum

$$S_{r_n,r_m}^{\alpha}(\nu) \triangleq \int_{\mathbb{R}} \int_{\mathbb{R}} \mathbb{E}\left\{ r_n^*(t) r_m(t+u) \right\} e^{-i2\pi(\alpha t + u\nu)} \mathrm{d}t \mathrm{d}u. \tag{49}$$

Since DSSS signals have several cycle frequencies, the set $\hat{\mathcal{A}}$ is very likely to contain several frequencies and may also be corrupted by false alarms inherent in any detection procedure. Therefore, $\hat{\mathcal{A}}$ must be further processed to provide a robust estimate of T_s. To do so, we suggest

finding the most likely greatest common divisor (GCD) of the estimated cycle frequencies based on the following three-step estimation procedure:

1) Make a list $\mathcal{D}_\alpha$ of all possible GCDs. This list is defined as the set of differences between the estimated cycle frequencies, that is

$$\mathcal{D}_{\hat{\alpha}} \triangleq \bigcup_{k=1}^{N_\alpha} \bigcup_{\ell=k+1}^{N_\alpha} \{|\hat{\alpha}_k - \hat{\alpha}_\ell|\} \tag{50}$$

where $\hat{\alpha}_k \in \mathcal{A}$ for all k and $N_\alpha = \text{card}\left(\hat{\mathcal{A}}\right)$.

2) For each candidate GCD $\Delta\hat{\alpha}_d \in \mathcal{D}_{\hat{\alpha}}$, count the number of cycle frequencies that are multiples of this value. Counting is performed as follows:

$$\begin{aligned} c(d) = \text{card}\Bigg(&\{k \in \{1,2,\ldots,N_\alpha\} : \hat{\alpha}_k \text{mod}\,(\Delta\hat{\alpha}_d) \leq \Delta\hat{\alpha}_d\epsilon\} \\ &\bigcup \{\ell \in \{1,2,\ldots,N_\alpha\} : \Delta\hat{\alpha}_d(1-\epsilon) \leq \hat{\alpha}_\ell \text{mod}\,(\Delta\hat{\alpha}_d)\} \Bigg). \end{aligned} \tag{51}$$

Since the cycle frequencies are estimated with a finite resolution, we allow for some tolerance $0 < \epsilon < 1$ when counting the multiples of $\Delta\hat{\alpha}_d$.

3) Estimate the symbol period as

$$\hat{T}_s = \frac{1}{\Delta\hat{\alpha}_{d^*}}, \tag{52}$$

where $d^* = \text{argmax}_d\, c(d)$.

This procedure is rather ad-hoc but, as illustrated next, works well in realistic contexts.

The performance of the symbol duration estimator is illustrated with replay simulations using real shallow-water channels. By convolving input signals with at-sea measurements of impulse responses, channel replay has become a standard procedure to test underwater communication systems [29], [58]–[61]. The impulse responses used in this section were measured by Sercel [62] off the coast of Lorient, France, in November 2021. The channel was probed in the $[60-190]$ Hz bandwidth, between a stationary source and a vertically suspended array with 3 hydrophones. Using the notations of Sec. IV-A, the geometry of transmission was the following: $r_s = 20$ km, z_s=10 m and $z_r = 12,\ 18,\ 30$ m for hydrophone 1, 2 and 3, respectively. The water depth was around 50 m. The channel was probed with a 10 s long linear chirp.[4] The spectrograms

[4]Note that other measurements performed during this experiment showed that the impulse response was very stable with a coherence-time greater than 30 s.

of the measured impulse responses along the array are shown in Fig. 16. Modal dispersion is clearly visible. As predicted by Eq. (38), the dispersion curves are identical for the three impulse responses and the amplitudes of each mode is depth-dependent. Moreover, the high-pass behavior discussed previously is observed, especially at the first hydrophone where mode 2 and 3 propagate a significant amount of acoustic energy.

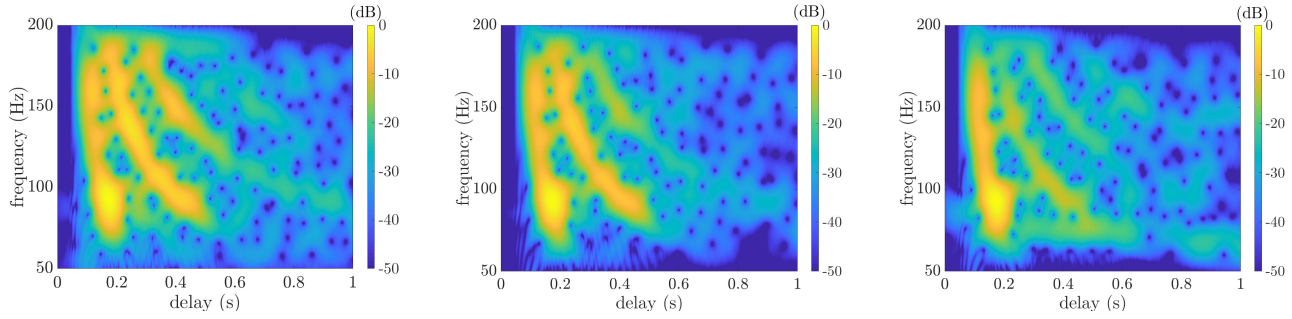

Fig. 16: Spectrograms of low-frequency impulse responses measured at-sea. (a): Hydrophone #1 ($z_r = 12$ m), Hydrophone #2 ($z_r = 18$ m), Hydrophone #3 ($z_r = 30$ m).

The channel input is a DSSS signal with QPSK symbols and a 15-chip spreading code. A root raised-cosine pulse is used with a roll-off factor $\xi = 1/4$. The symbol duration is set to $T_s \approx 153.8$ ms, which corresponds to a symbol rate of 6.5 Bd and a chip rate of 97.5 Hz. The duration of the received signal is set to $T_{\text{obs}} = 15$ s. All simulations are performed with a spatially uncorrelated additive white Gaussian noise. Results are examined versus the in-band SNR defined as

$$\text{SNR} = \frac{\sum_{n=1}^{N_h} E_b^{(n)}}{N_h N_0} \times \frac{2T_c}{T_s\,(1+\xi)}, \tag{53}$$

where T_c is the chip duration and $E_b^{(n)}$ denotes the energy per bit at the n-th hydrophone. The detection threshold Λ^{DC} in Eq. (47) is set such that the false-alarm rate in noise-only conditions is 0.5%. Since most of these false-alarms will be removed by the post-processing procedure described previously, this rate better not be too low to limit the number of missed detections. The tolerance ϵ in Eq. (51) is set to 5% and the spectral cross-coherence density $\hat{C}^{\alpha}_{r_n,r_m}(\nu)$ is estimated using time-smoothed averaged cyclic periodograms. The sampling rate is chosen greater than 4 times the chip rate and is random. This choice is made to avoid favorable

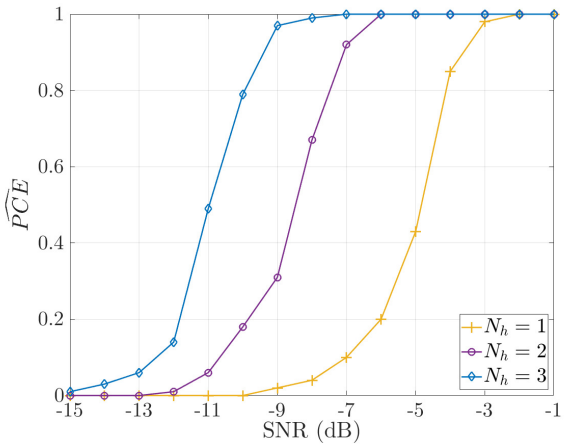

Fig. 17: Correct estimation rate of the DSSS symbol duration as a function of SNR.

conditions where the sampling rate is a multiple of $1/T_s$. The performance is evaluated in terms of probability of correct estimation (PCE), which is defined as the probability that the relative estimation error is less than 1%, that is

$$\text{PCE} = \mathbb{P}\left(\left|\frac{\hat{T}_s - T_s}{T_s}\right| \leq 10^{-2}\right). \tag{54}$$

For each SNR, this probability is estimated with 100 Monte-Carlo trials.

The results are shown in Fig. 17 as a function of SNR for $N_h = 1, 2$ and 3. Whatever the configuration, good results are achieved for negative SNRs. Moreover, array processing provides a significant performance gain. For instance, a 6 dB improvement is achieved by using 3 hydrophones instead of one. Such a result is expected in shallow-water since the spatial coherence along the vertical array is usually very high at low-frequencies [63]. Finally, the high-pass behavior of modal propagation does not affect much this experiment. This is illustrated in Fig. 18-(a) where an example of the test statistic in Eq. (47) is plotted before and after thresholding. For ease of interpretation, a grid is displayed with a step set to $1/T_s = 6.5$ Hz. We see a few false alarms but, more importantly, we see that more than 10 cycle frequencies are correctly detected. As shown by the results of Eqs (51) and (52) displayed in Fig. 18-(b), this is large enough to correctly estimate the symbol duration.

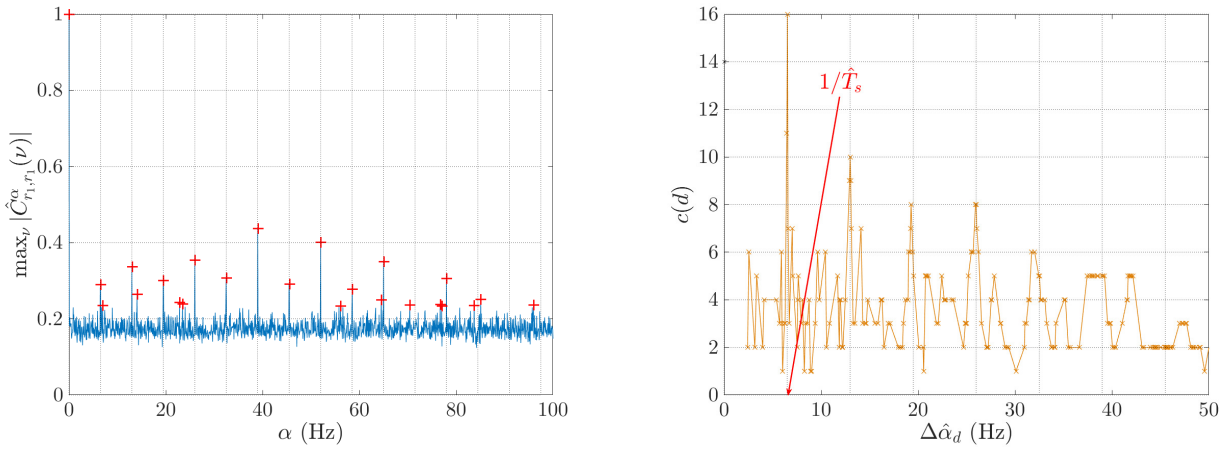

(a) (b)

Fig. 18: Illustration of the method used to estimate the symbol duration of a DSSS signal, $N_h = 1$ and SNR $= 0$ dB. (a) Test statistic of Eq. (47) before (plain line) and after thresholding (crosses), (b) plot of Eqs (51) and (52).

V. Conclusions

The theoretical results derived in this paper as well as their applications on simulated and real data confirm the potential of cyclostationary-based methods for underwater acoustic communications. They also show that off-the-shelf RF methods are not always relevant for underwater channels. For instance, Doppler scaling, as encountered in typical high-frequency multiscale-multilag channels, transforms cyclostationary processes into time-warped cyclostationary ones. As discussed in Sec. III, this time-warping may be either exploited to estimate the Doppler scale or compensated somehow to recover the underlying cyclic features. By applying proper approximations, specific to underwater scenarios, it is shown that recovering these features can be simple and may not require any resampling procedure. Unlike multiscale-multilag channels, low frequency dispersive channels do not severely alter the cyclostationary properties of communication signals. This means that the standard statistical framework can be used to model and estimate the cycle frequencies at the output of such a channel. However, it should be emphasized that modal propagation can have a high-pass filter behavior. Therefore, dispersive channels may significantly attenuate the higher cycle frequencies. Moreover, the frequency

dependency of the modes travel-time shifts and spreads the amplitude of the cyclic autocorrelation function along the time-lag axis.

By addressing the problems of Doppler scale estimation, signal detection and symbol-rate estimation, this paper only provides a brief overview of what could be achieved with cyclostationary-based methods. For instance, some acoustic interference, such as propeller noise or clicks from odontocetes, are known to be cyclostationary. They could possibly be mitigated using FRESH-like filters [64] or source separation methods [65] to improve the robustness of communication links. Similarly, the non-data-aided estimation of dispersive channels using opportunistic cyclostationary signals [2, Sec. 10] may be a relevant input to solve inverse problems such as matched-mode processing [66]. The range of possible applications is vast. Finally, the proposed analysis is restricted to second-order statistics but could also be extended to higher orders to exploit additional information [67].

VI. Acknowledgment

The author would like to thank Christophe Laot for providing the experimental data used in Sec. III-D as well as Sercel for conducting the low-frequency experiment described in Sec. IV-C.

APPENDIX A
EXAMPLES OF CYCLOSTATIONARY COMMUNICATION SIGNALS

A. PSK/QAM

Let $x(t)$ be the complex envelope of a PSK or QAM signal. It can be expressed as

$$x(t) \triangleq \sum_{k\in\mathbb{Z}} b_k g\left(t - kT_s\right), \tag{55}$$

where b_k denotes the k-th data symbol, $g(\cdot)$ is the pulse-shaping filter and T_s is the symbol duration. The symbols b_k are assumed to be zero-mean, identically and independently distributed (i.i.d). The bandwidth of $x(t)$ is defined as the interval $[-(1+\xi)/(2T_s), (1+\xi)/(2T_s)]$, where ξ is the excess bandwidth of the filter g.

PSK/QAM signals are known to be cyclostationary with period T_s. Their autocorrelation function satisfies [2, Sec. 5.2]

$$R_x(t,u) = \sum_{n\in\mathbb{Z}} R_x^{\frac{n}{T_s}}(u) e^{i2\pi\frac{n}{T_s}t}, \tag{56}$$

where

$$R_x^{\frac{n}{T_s}}(u) = \frac{\mathbb{E}\left\{|b_k|^2\right\}}{T_s}\int_{\mathbb{R}} g^*(t)g(t+u)e^{-i2\pi\frac{n}{T_s}t}\mathrm{d}t. \tag{57}$$

In practice, pulse-shaping filters used in underwater communications are real-valued. Thus, the cyclic-autocorrelation function also satisfies

$$R_x^{\frac{n}{T_s}}(u) = \frac{\mathbb{E}\left\{|b_k|^2\right\}}{T_s}(G \circledast \tilde{G}_u)\left(\frac{n}{T_s}\right), \tag{58}$$

where $\tilde{G}_u(\nu) = G(\nu)e^{i2\pi\nu u}$ and $\circledast$ denotes convolution. Practical values for the excess bandwidth ξ are restricted to the interval $(0,1)$. For these values, $(G \circledast \tilde{G}_u)\left(\frac{n}{T_s}\right)$ is null for $|n| > 1$. Therefore, n is restricted to the set $\{-1,0,1\}$ and Eq. (56) becomes

$$R_x(t,u) = R_x^0(u) + 2\Re\left(R_x^{\frac{1}{T_s}}(u)\right)\cos\left(2\pi\frac{t}{T_s}\right) - 2\Im\left(R_x^{\frac{1}{T_s}}(u)\right)\sin\left(2\pi\frac{t}{T_s}\right). \tag{59}$$

From Eqs (4), (5) and (57), it can be shown that the spectral correlation function and the cyclic spectrum of PSK/QAM signals satisfy [2, Sec. 5.2]

$$S_x\left(\nu_1,\nu_2\right) = \frac{\mathbb{E}\left\{|b_k|^2\right\}}{T_s}\sum_{n=-1}^{1} G\left(\nu_2\right)G^*\left(\nu_2 - \frac{n}{T_s}\right)\delta\left(\nu_1 - \nu_2 + \frac{n}{T_s}\right), \tag{60}$$

and

$$S_x^{\alpha}\left(\nu\right) = \frac{\mathbb{E}\left\{|b_k|^2\right\}}{T_s}\sum_{n=-1}^{1} G\left(\nu\right)G^*\left(\nu-\alpha\right)\delta_{[\alpha T_s - n]}, \tag{61}$$

where $\delta_{[\cdot]}$ denotes the Kronecker delta. An illustration of the cyclostationary features of a PSK/QAM signal is shown in Fig. 19.

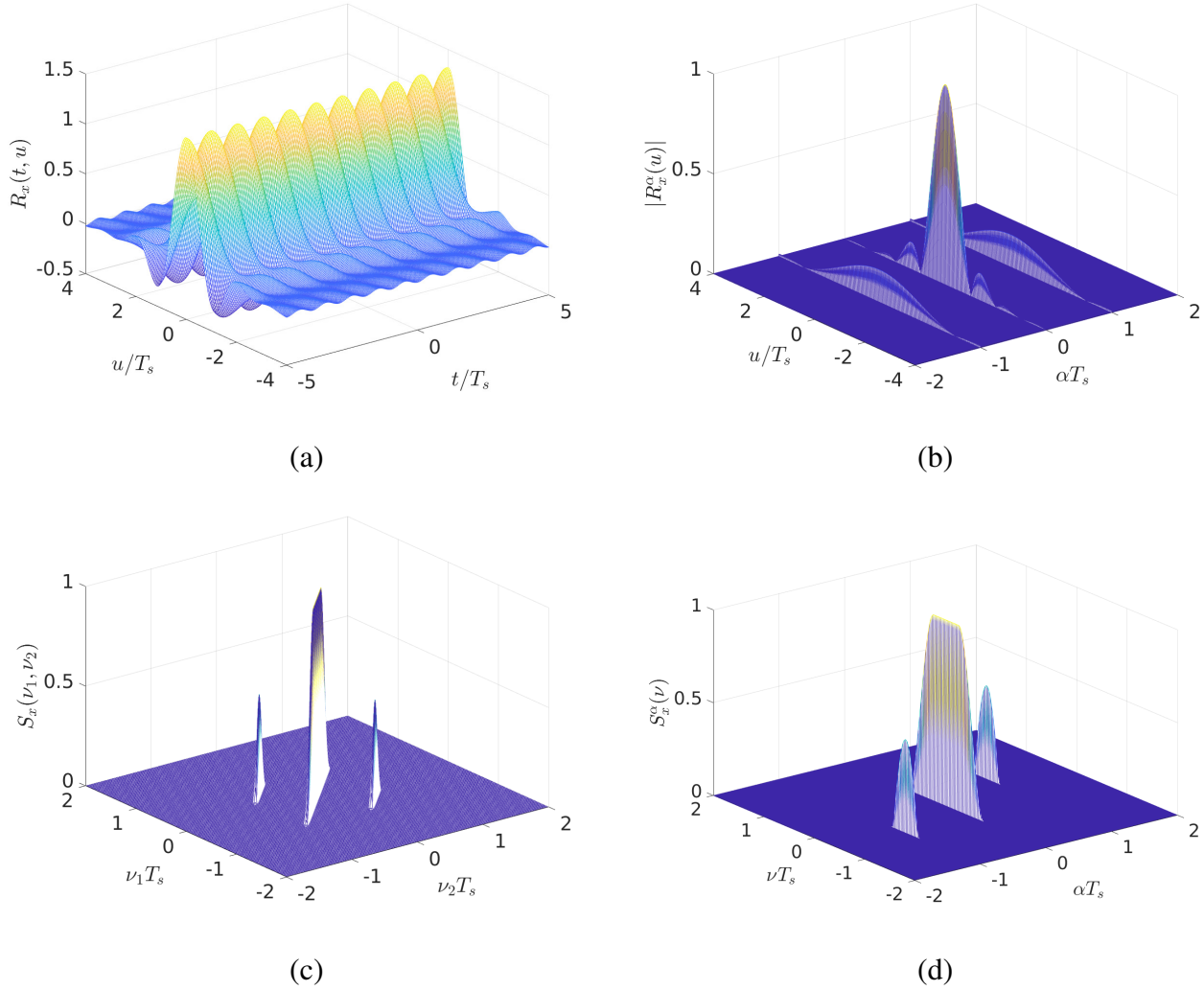

Fig. 19: Illustration of the cyclostationary features of a PSK/QAM signal with a root-raised-cosine filter g with $\xi = 0.5$. (a) Autocorrelation function, (b) cyclic autocorrelation function, (c) spectral correlation function, (d) cyclic spectrum.

B. OFDM

An OFDM signal with N subcarriers can be expressed as

$$x(t) \triangleq \frac{1}{\sqrt{N}} \sum_{k\in\mathbb{Z}} \sum_{n=0}^{N-1} b_{k,n} e^{2i\pi n\Delta_f (t-T_g-kT_s)} g(t-kT_s), \tag{62}$$

where $b_{k,n}$ is the data symbol at the n-th subcarrier of the k-th OFDM symbol. Δ_f denotes the subcarrier spacing, T_s is the total symbol duration, $T_g \triangleq T_s - 1/\Delta_f$ is the guard-time and g is the real-valued pulse-shaping filter (or window). Three main types of OFDM signals are used in underwater acoustics [19], [21], [22]: zero-padded OFDM (ZP-OFDM), cyclic prefix OFDM (CP-OFDM), and guard-free OFDM with super-imposed pilots (SIP-OFDM). Let $\text{supp}(\cdot)$ denote the support of a function, these OFDM signals can be described by the following set of parameters

- ZP-OFDM: $T_g \neq 0$, $\text{supp}(g) = [0, T_s - T_g)$, $b_{k,n}$ zero-mean and i.i.d,
- CP-OFDM: $T_g \neq 0$, $\text{supp}(g) = [0, T_s)$, $b_{k,n}$ zero-mean and i.i.d,
- SIP-OFDM: $T_g = 0$, $\text{supp}(g) = [0, T_s)$, $b_{k,n} = b_n^p + ib_{k,n}^d$, where b_n^p are deterministic pilots identical for all OFDM symbols and $b_{k,n}^d$ are zero-mean, i.i.d data symbols.

Each type of OFDM signal exhibits some periodicity in their second-order statistics. It results from the periodic use of a guard-time for ZP-OFDM, from the redundancy induced by the cyclic prefix for CP-OFDM and from the correlation of the pilot sequence b_n^p for SIP-OFDM. More specifically, their cyclostationary features are highlighted by the following results.

1) ZP-OFDM and CP-OFDM: Based on Eq. (62), it can be shown that the autocorrelation function satisfies

$$R_x(t,u) = \begin{cases} \mathbb{E}\left\{|b_{k,n}|^2\right\} \frac{\sin\left(\pi\Delta_f N u\right)}{N\sin\left(\pi\Delta_f u\right)} e^{i\pi\Delta_f(N-1)u} & \\ \times \sum_{\ell\in\mathbb{Z}} g(t-\ell T_s)g(t+u-\ell T_s), & 0 < |u| < T_s \\ \mathbb{E}\left\{|b_{k,n}|^2\right\} \sum_{\ell\in\mathbb{Z}} g^2(t-\ell T_s), & u = 0 \\ 0 & \text{otherwise.} \end{cases} \tag{63}$$

By Fourier transforming $R_x(t,u)$ with respect to t, we get the expression of the cyclic autocorrelation function

$$R_x^\alpha(u) = \begin{cases} \mathbb{E}\left\{|b_{k,n}|^2\right\} \frac{\sin\left(\pi\Delta_f N u\right)}{N\sin\left(\pi\Delta_f u\right)} e^{i\pi\Delta_f(N-1)u} & \\ \times \delta_{[(\alpha T_s) \bmod 1]} \frac{1}{T_s} \int_0^{T_s} g(t)g(t+u)e^{-i2\pi\alpha t}\mathrm{d}t, & 0 < |u| < T_s \\ \mathbb{E}\left\{|b_{k,n}|^2\right\} \delta_{[(\alpha T_s) \bmod 1]} \frac{1}{T_s} \int_0^{T_s} g^2(t)e^{-i2\pi\alpha t}\mathrm{d}t, & u = 0 \\ 0 & \text{otherwise,} \end{cases} \tag{64}$$

where mod denotes the modulo operation. The spectral autocorrelation function and the cyclic spectrum are obtained by noticing that the Fourier transform of $x(t)$ can be expressed as

$$X(\nu) = \frac{1}{\sqrt{N}} \sum_{k\in\mathbb{Z}} \sum_{n=0}^{N-1} b_{k,n} G(\nu - n\Delta_f) e^{-i2\pi k T_s \nu} e^{-i2\pi n\Delta_f(T_g + kT_s)}. \tag{65}$$

It then follows that

$$S_x\left(\nu_1,\nu_2\right)=\frac{\mathbb{E}\left\{|b_{k,n}|^2\right\}}{T_sN}\sum_{\ell\in\mathbb{Z}}\sum_{m=0}^{N-1}G\left(\nu_2-m\Delta_f\right)G^*\left(\nu_2-m\Delta_f-\frac{\ell}{T_s}\right)\delta\left(\nu_1-\nu_2+\frac{\ell}{T_s}\right) \tag{66}$$

and

$$S_x^\alpha\left(\nu\right)=\frac{\mathbb{E}\left\{|b_{k,n}|^2\right\}}{T_sN}\delta_{[(\alpha T_s)\text{mod}1]}\sum_{m=0}^{N-1}G\left(\nu-m\Delta_f\right)G^*\left(\nu-m\Delta_f-\alpha\right). \tag{67}$$

Both ZP and CP-OFDM are cyclostationary with period T_s. An illustration of the cyclostationary features of a ZP-OFDM signal with a rectangular window is shown in Fig. 20.

2) SIP-OFDM: Based on the definition given previously, SIP-OFDM signals can be expressed as $x(t)=x_p(t)+ix_d(t)$ where $x_p(t)$ and $x_d(t)$ are obtained by replacing $b_{k,n}$ in Eq. (62) with b_n^p and $b_{k,n}^d$, respectively. Since the data symbols $b_{k,n}$ are zero-mean, the second-order statistics of $x(t)$ can be expressed as the sum of the individual statistics of $x_p(t)$ and $x_d(t)$. For instance, the cyclic autocorrelation function can be written as

$$R_x^\alpha(u)=R_{x_p}^\alpha(u)+R_{x_d}^\alpha(u), \tag{68}$$

where $R_{x_d}^\alpha$ is obtained by setting $T_g=0$, $\Delta_f=1/T_s$ in Eq. (64) and by replacing $b_{k,n}$ with $b_{k,n}^d$. The autocorrelation function of the pilots is periodic in t with period T_s and its cyclic autocorrelation function is also periodic in u with period T_s. They satisfy

$$R_{x_p}(t,u)=\frac{1}{N}\sum_{k\in\mathbb{Z}}\sum_{k'\in\mathbb{Z}}\sum_{n=0}^{N-1}\sum_{n'=0}^{N-1}b_n^{p^*}b_{n'}^p e^{2i\pi(n'-n)t/T_s}e^{2i\pi n'u/T_s}g(t-kT_s)g(t+u-k'T_s), \tag{69}$$

and

$$R_{x_p}^\alpha(u)=\frac{1}{N}\delta_{[(\alpha T_s)\text{mod}1]}\sum_{n=0}^{N-1}\sum_{n'=0}^{N-1}b_n^{p^*}b_{n'}^p\sum_{k\in\mathbb{Z}}q_{n,n'}^\alpha(u-kT_s), \tag{70}$$

where

$$q_{n,n'}^\alpha(u)=\frac{1}{T_s}\int_0^{T_s}g(t)g(t+u)e^{-2i\pi t(\alpha+(n-n')/T_s)}e^{2i\pi n'u/T_s}\text{d}t. \tag{71}$$

Based on Eq. (68), the cyclic spectrum can be expressed as

$$S_x^\alpha\left(\nu\right)=S_{x_p}^\alpha(\nu)+S_{x_d}^\alpha(\nu), \tag{72}$$

where $S_{x_p}^\alpha(\nu)$ is obtained by noticing that $q_{n,n'}^\alpha(u)=\left(\frac{1}{T_s}g(u)e^{2i\pi n'u/T_s}\right)\circledast\left(g(-u)e^{2i\pi(\alpha+nu/T_s)}\right)$ and by Fourier transforming $R_{x_p}^\alpha(u)$ with respect to u, that is

$$S_{x_p}^\alpha(\nu)=\frac{1}{T_s^2N}\delta_{[(\alpha T_s)\text{mod}1]}\sum_{n=0}^{N-1}\sum_{n'=0}^{N-1}b_n^{p^*}b_{n'}^pG\left(\nu-\frac{n'}{T_s}\right)G^*\left(\nu-\frac{n}{T_s}-\alpha\right)\sum_{k\in\mathbb{Z}}\delta\left(\nu-\frac{k}{T_s}\right). \tag{73}$$

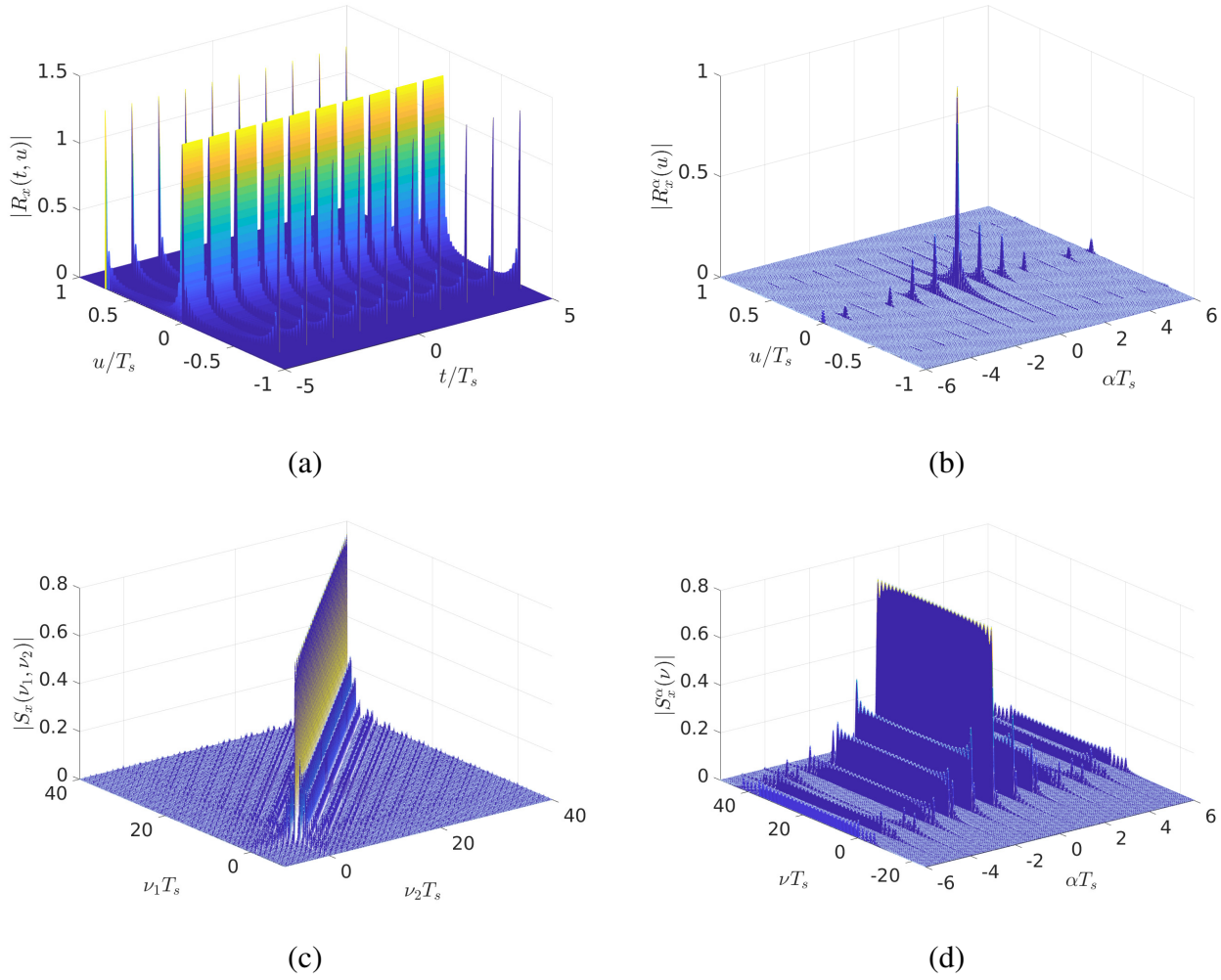

Fig. 20: Illustration of the cyclostationary features of a ZP-OFDM signal with $T_s = T_s/4$, $N = 32$ and a rectangular window. (a) Autocorrelation function, (b) cyclic autocorrelation function, (c) spectral correlation function, (d) cyclic spectrum.

C. DSSS

Most DSSS signals used for underwater acoustic communications can be expressed as [16]–[18]

$$x(t) \triangleq \sum_{k\in\mathbb{Z}} \sum_{n=0}^{N_c-1} b_k c_n g\left(t - nT_c - kT_s\right), \tag{74}$$

where b_k denotes the zero-mean i.i.d. data symbols, c_n is the N_c-length deterministic spreading sequence and $g(\cdot)$ is the real-valued pulse-shaping filter. T_s denotes the symbol duration and T_c

is the chip period such that $T_s = N_c T_c$. Such a signal is often referred to as a short-code DSSS signal as opposed to long-code signals which use a spreading sequence longer than a single symbol.

Short-code DSSS signals are known to be cyclostationary with period T_s. They satisfy the following results [68]:

- Autocorrelation function:

$$R_x(t,u) = \mathbb{E}\left\{|b_{k,n}|^2\right\} \sum_{k\in\mathbb{Z}} \sum_{n=0}^{N_c-1} \sum_{n'=0}^{N_c-1} c_n^* c_{n'} g\left(t - nT_c - kT_s\right) g\left(t + u - n'T_c - kT_s\right). \quad (75)$$

- Cyclic autocorrelation function:

$$R_x^\alpha(u) = \mathbb{E}\left\{|b_{k,n}|^2\right\} \delta_{[(\alpha T_s) \bmod 1]} r_g^\alpha(u) \circledast \gamma_c^\alpha(u) \quad (76)$$

where

$$r_g^\alpha(u) \triangleq \frac{1}{T_s} \int_{\mathbb{R}} g(t) g(t+u) e^{-i2\pi\alpha t} \mathrm{d}t \quad (77)$$

and

$$\gamma_c^\alpha(u) \triangleq \sum_{n=0}^{N_c-1} \sum_{n'=0}^{N_c-1} c_n^* c_{n'} e^{-i2\pi\alpha n T_c} \delta\left(u - (n'-n)T_c\right). \quad (78)$$

- Spectral correlation function:

$$\begin{aligned} S_x\left(\nu_1, \nu_2\right) = \frac{\mathbb{E}\left\{|b_{k,n}|^2\right\}}{T_s} \sum_{\ell\in\mathbb{Z}} \sum_{m=0}^{N-1} & G\left(\nu_2\right) G^*\left(\nu_2 - \frac{\ell}{T_s}\right) \\ & \times C\left(\nu_2\right) C^*\left(\nu_2 - \frac{\ell}{T_s}\right) \delta\left(\nu_1 - \nu_2 + \frac{\ell}{T_s}\right) \end{aligned} \quad (79)$$

where $C\left(\nu\right) = \sum_{n=0}^{N_c-1} c_n e^{-i2\pi\nu n T_c}$.

- Cyclic spectrum:

$$S_x^\alpha(\nu) = \frac{\mathbb{E}\left\{|b_{k,n}|^2\right\}}{T_s} \delta_{[(\alpha T_s) \bmod 1]} G\left(\nu\right) G^*\left(\nu - \alpha\right) C\left(\nu\right) C^*\left(\nu - \alpha\right). \quad (80)$$

As illustrated in Fig. 21, DSSS signals can be easily distinguished from PSK/QAM signals by their cyclic properties. As discussed previously, PSK/QAM signals have only three cycle frequencies ($\alpha = -1/T_s, 0, 1/T_s$) whereas DSSS signals have many more. This difference comes from the pulse shaping filter g. For DSSS, it is equal to the spreading sequence shaped by the chip pulse which is designed with respect to the duration T_c rather than T_s. Therefore, the larger N_c is, the higher the number of cycle frequencies will be.

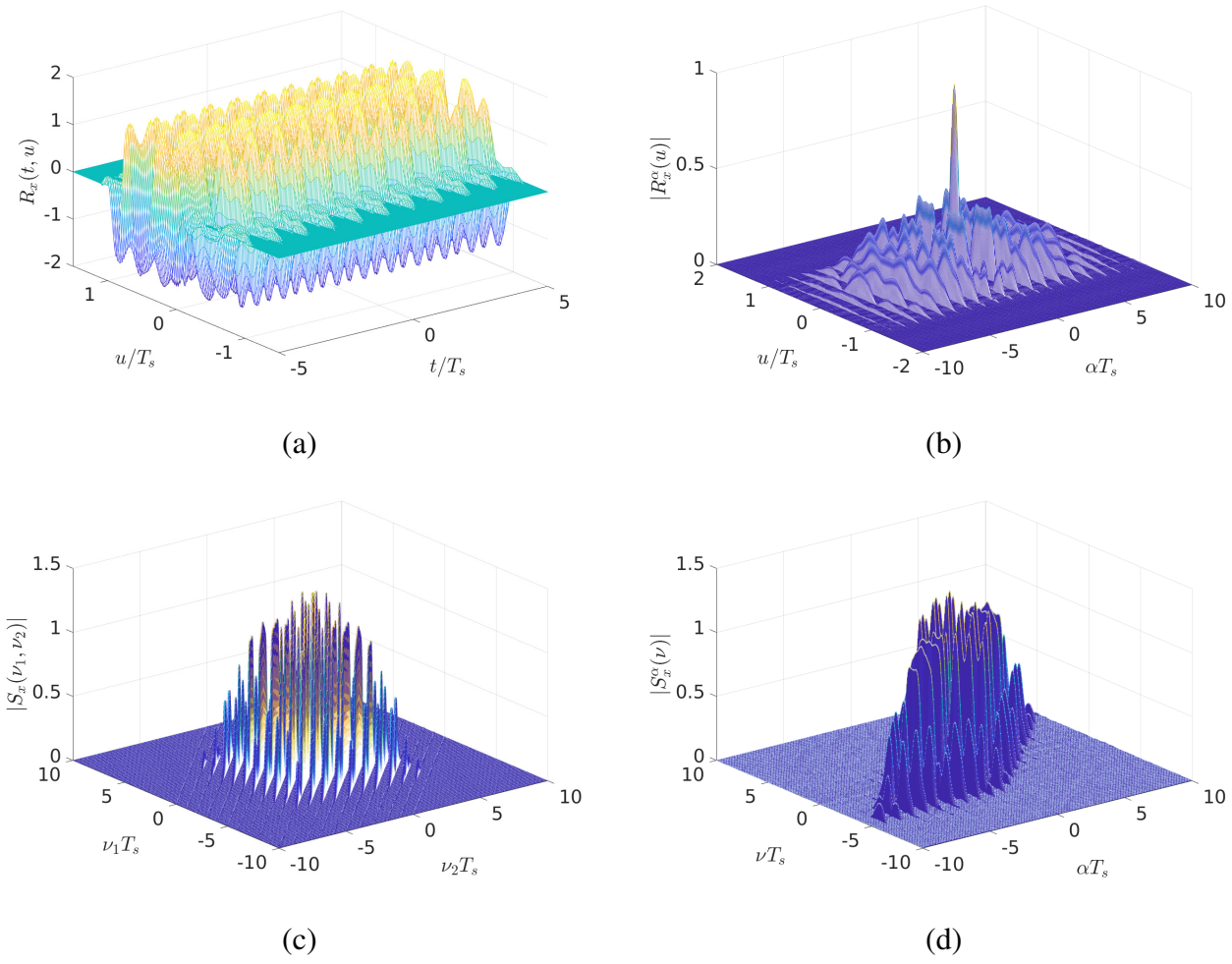

Fig. 21: Illustration of the cyclostationary features of a DSSS signal with a maximum-length spreading sequence, $N_c = 7$, root-raised-cosine filter g with $\xi = 0.5$. (a) Autocorrelation function, (b) cyclic autocorrelation function, (c) spectral correlation function, (d) cyclic spectrum.

APPENDIX B
RELATIONSHIPS BETWEEN $R_x^\alpha(u)$ AND $R_{y_\ell}(t,u)$

From Eqs. (1), (2) and (7), $R_{y_\ell}(t,u)$ can be expressed as function of a $R_x^\alpha(u)$ as follows

$$\begin{aligned} R_{y_\ell}(t,u) &= e^{i2\pi f_c(\psi_\ell(t+u)-\psi_\ell(t)-u)}\mathbb{E}\left\{x^*(\psi_\ell(t)-\tau_\ell)x(\psi_\ell(t+u)-\tau_\ell)\right\} \\ &= e^{i2\pi f_c(\psi_\ell(t+u)-\psi_\ell(t)-u)}\sum_{\alpha\in\mathcal{A}} R_x^\alpha(\psi_\ell(t+u)-\psi_\ell(t))e^{i2\pi\alpha(\psi_\ell(t)-\tau_\ell)} \\ &= e^{i2\pi f_c(\phi_\ell(t,u)-u)}\sum_{\alpha\in\mathcal{A}} R_x^\alpha(\phi_\ell(t,u))e^{i2\pi\alpha(\psi_\ell(t)-\tau_\ell)} \end{aligned} \tag{81}$$

with $\phi_\ell(t,u) \triangleq \psi_\ell(t+u) - \psi_\ell(t)$.

$R_x^\alpha(u)$ can also be expressed as a function of $R_{y_\ell}(t,u)$. First, let

$$\psi_\ell^{-1}(t) = \begin{cases} \frac{c}{a_\ell}\left(1 - \frac{v_\ell}{c} \pm \sqrt{-\frac{2ta_\ell}{c} + \left(1-\frac{v_\ell}{c}\right)^2}\right) & \text{if } a_\ell \neq 0, \\ \frac{ct}{c-v_\ell} & \text{otherwise} \end{cases} \tag{82}$$

be the inverse function of $\psi_\ell(t)$ and

$$\rho(t, t+u) \triangleq R_{y_\ell}(t,u) e^{-i2\pi f_c(\phi_\ell(t,u)-u)}. \tag{83}$$

Using Eq. (81), we obtain $\rho\left(\psi_\ell^{-1}(t), \psi_\ell^{-1}(t+u)\right) = \sum_{\beta\in\mathcal{A}} R_x^\beta(u) e^{i2\pi\beta(t-\tau_\ell)}$. Therefore,

$$\lim_{T\to\infty} \frac{e^{i2\pi\alpha\tau_\ell}}{T} \int_{-\frac{T}{2}}^{\frac{T}{2}} \rho(\psi_\ell^{-1}(t), \psi_\ell^{-1}(t+u)) e^{-i2\pi\alpha t}\mathrm{d}t = \sum_{\beta\in\mathcal{A}} R_x^\beta(u) e^{i2\pi(\alpha-\beta)\tau_\ell} \lim_{T\to\infty} \frac{1}{T} \int_{-\frac{T}{2}}^{\frac{T}{2}} e^{-i2\pi(\alpha-\beta)t}\mathrm{d}t. \tag{84}$$

Since

$$\frac{1}{T}\int_{-\frac{T}{2}}^{\frac{T}{2}} e^{-i2\pi(\alpha-\beta)t}\mathrm{d}t = \begin{cases} 1 & \text{if } \alpha = \beta, \\ \text{sinc}\left(\pi T(\alpha-\beta)\right) & \text{otherwise,} \end{cases} \tag{85}$$

we conclude that

$$\lim_{T\to\infty} \frac{e^{i2\pi\alpha\tau_\ell}}{T} \int_{-\frac{T}{2}}^{\frac{T}{2}} \rho\left(\psi_\ell^{-1}(t), \psi_\ell^{-1}(t+u)\right) e^{-i2\pi\alpha t}\mathrm{d}t = R_x^\alpha(u). \tag{86}$$

APPENDIX C
SPECTRAL CORRELATION FUNCTION IN MSML CHANNELS WITH NO ACCELERATION

The Fourier transform of $y_\ell(t)$ satisfies

$$Y_\ell(\nu) = \int_{\mathbb{R}} x(\psi_\ell(t) - \tau_\ell) e^{i2\pi f_c(\psi_\ell(t)-\tau_\ell)} e^{-i2\pi t(\nu+f_c)}\mathrm{d}t. \tag{87}$$

If $a_\ell = 0$, the spectral correlation function of $y_\ell(t)$ exists and can be expressed as

$$\begin{aligned} S_{y_\ell}(\nu_1,\nu_2) &= \iint_{\mathbb{R}^2} \mathbb{E}\left\{x^*(\psi_\ell(t_1)-\tau_\ell)x(\psi_\ell(t_2)-\tau_\ell)\right\} e^{i2\pi f_c(\psi_\ell(t_2)-\psi_\ell(t_1))} \\ &\qquad \times e^{-i2\pi(t_2(\nu_2+f_c)-t_1(\nu_1+f_c))}\mathrm{d}t_1\mathrm{d}t_2 \\ &= \iint_{\mathbb{R}^2} \sum_{\alpha\in\mathcal{A}} R_x^\alpha\left(\left(1-\frac{v_\ell}{c}\right)u\right) e^{i2\pi\alpha\left((1-\frac{v_\ell}{c})t-\tau_\ell\right)} e^{i2\pi f_c\left((1-\frac{v_\ell}{c})u\right)} \\ &= \qquad \times e^{-i2\pi((t+u)(\nu_2+f_c)-t(\nu_1+f_c))}\mathrm{d}u\mathrm{d}t \\ &= \iint_{\mathbb{R}^2} \sum_{\alpha\in\mathcal{A}} R_x^\alpha\left(\left(1-\frac{v_\ell}{c}\right)u\right) e^{-i2\pi u\left(\nu_2+f_c\frac{v_\ell}{c}\right)} e^{i2\pi\alpha\left((1-\frac{v_\ell}{c})t-\tau_\ell\right)} e^{-i2\pi t(\nu_2-\nu_1)}\mathrm{d}u\mathrm{d}t \\ &= \frac{c}{|c-v_\ell|}\sum_{\alpha\in\mathcal{A}} S_x^\alpha\left(\frac{c\nu_2+f_cv_\ell}{c-v_\ell}\right)\delta\left(\nu_1-\nu_2+\alpha\left(1-\frac{v_\ell}{c}\right)\right)e^{-i2\pi\alpha\tau_\ell}. \end{aligned} \tag{88}$$

Eq. (17) then results from the WSS channel and WSS noise assumptions, as well as from the combination of Eqs (6) and (88).

APPENDIX D
IMPLEMENTATION OF THE DOPPLER SCALE ESTIMATOR

In practice, the received signal $r(t)$ is sampled at a frequency f_s so that N_{obs} discrete-time samples are available over the duration T_{obs}. The sampling frequency f_s must be chosen to avoid aliasing in both cyclic and spectral frequency domain. For any band-limited signal with monolateral bandwidth B, a sufficient condition to avoid this aliasing is to choose $f_s \geq 4B$ [2, Eq. (3.112)]. The discrete-time estimate of the cost function (23) is

$$\hat{J}_r(\mu_1, \mu_2) = \frac{1}{N_{\text{obs}}} \left| \sum_{k=0}^{N_{\text{obs}}-1} |r(k/f_s)|^2 e^{-i\frac{2\pi}{T_s f_s^2}(\mu_1 k f_s + \mu_2 k^2)} \right|^2 . \tag{89}$$

Following an analysis similar to the one presented in [69], it can be shown that a consistent estimator of (μ_1, μ_2) is obtained by maximizing $\hat{J}_r$. As illustrated in Fig. 4, this cost is not convex. A two-step optimization procedure is therefore applied. First, a coarse maximization is performed using a grid search. The search interval is based on physical considerations of maximum velocity and acceleration. For instance, by assuming a maximum velocity of 10 m.s^{-1}, a maximum acceleration of 1 m.s^{-2} and by considering that the sound speed is around 1500 m.s^{-1}, from Eq. (7), we get the following bounds: $\mu_1^{\min} \leq \mu_1 \leq \mu_1^{\max}$, with $\mu_1^{\min} = 1 - 2/3.10^{-2}$ and $\mu_1^{\max} = 1 + 2/3.10^{-2}$, and $|\mu_2| \leq 1/3.10^{-3}$. The choice of the grid step mostly depends on T_{obs}. For larger T_{obs}, the mainlobe of $\hat{J}_r$ gets sharper and the step must be smaller. Eq. (89) can be implemented very efficiently by representing it as a chirp Z-transform [70]. More specifically, for any $\mu_{1,n} = \mu_1^{\min} + n\Delta_{\mu_1}$, $n = 0, \cdots, N_{\mu_1} - 1$, where Δ_{μ_1} is the grid step for μ_1 and N_{μ_1} is the number of grid points, we have

$$\hat{J}_r(\mu_{1,n}, \mu_2) = \frac{1}{N_{\text{obs}}} \left| \sum_{k=0}^{N_{\text{obs}}-1} s_{\mu_1,\mu_2}(k) z_n^{-k} \right|^2 , \tag{90}$$

where $s_{\mu_1,\mu_2}(k) = |r(k/f_s)|^2 e^{-i\frac{2\pi}{T_s f_s^2}(\mu_1^{\min} f_s + \mu_2 k^2)}$ and $z_n = e^{i\frac{2\pi\Delta_{\mu_1}}{T_s f_s} n}$. Therefore, for a fixed value of μ_2, the N_{μ_1} values of $\hat{J}_r(\mu_{1,n}, \mu_2)$ can be computed in $\mathcal{O}\left(N_{\text{obs}} \log(N_{\text{obs}})\right)$ operations using an FFT-based implementation.

After the coarse-grid search, a gradient-ascent approach can be applied to get more precise results. Let $\boldsymbol{\mu} \triangleq [\mu_1, \mu_2]^T$ and $\nabla_{\boldsymbol{\mu}} \triangleq [\partial/\partial_{\mu_1}, \partial/\partial_{\mu_2}]^T$, it can be shown that the gradient of the cost function (23) satisfies

$$\nabla_{\boldsymbol{\mu}} J_r(\boldsymbol{\mu}) = \frac{2}{T_{\text{obs}}^2} \Re \left\{ \int_0^{T_{\text{obs}}} |r(t)|^2 e^{i\frac{2\pi}{T_s}(\mu_1 t + \mu_2 t^2)} \mathrm{d}t \int_0^{T_{\text{obs}}} |r(t)|^2 \left(-i\frac{2\pi}{T_s}[t, t^2]^T \right) e^{-i\frac{2\pi}{T_s}(\mu_1 t + \mu_2 t^2)} \mathrm{d}t \right\}. \tag{91}$$

At iteration $j+1$, the estimate of $\boldsymbol{\mu}$ is obtained as

$$\hat{\boldsymbol{\mu}}^{(j+1)} = \hat{\boldsymbol{\mu}}^{(j)} + \kappa(j) \widehat{\nabla}_{\boldsymbol{\mu}} J_r(\boldsymbol{\mu})|_{\boldsymbol{\mu}=\hat{\boldsymbol{\mu}}^{(j)}}, \tag{92}$$

where $\widehat{\nabla}_{\boldsymbol{\mu}} J_r(\boldsymbol{\mu})$ is the discrete-time approximation of (91) and $\kappa(j)$ is the step size at iteration j. $\hat{\boldsymbol{\mu}}^{(0)}$ is the result of the coarse-grid search and $\kappa(j)$ is computed using the Barzilai Borwein approach [71]

$$\kappa(j) = \frac{\left| \left(\hat{\boldsymbol{\mu}}^{(j)} - \hat{\boldsymbol{\mu}}^{(j-1)} \right)^T \left(\widehat{\nabla}_{\boldsymbol{\mu}} J_r\left(\boldsymbol{\mu}^{(j)}\right) - \widehat{\nabla}_{\boldsymbol{\mu}} J_r\left(\boldsymbol{\mu}^{(j-1)}\right) \right) \right|}{\left\| \widehat{\nabla}_{\boldsymbol{\mu}} J_r\left(\boldsymbol{\mu}^{(j)}\right) - \widehat{\nabla}_{\boldsymbol{\mu}} J_r\left(\boldsymbol{\mu}^{(j-1)}\right) \right\|^2}. \tag{93}$$

APPENDIX E
IMPLEMENTATION OF THE APPROXIMATED DE-WARPED CYCLOSTATIONARY STATISTIC

Using the same notations and assumptions as in Appendix D, the discrete-time implementation of cost function (35) is

$$\hat{J}_r^{\text{ADCS}} = \max_{(\mu_1,\mu_2)} \frac{1}{N_{\text{obs}}} \sum_{(u,\alpha)\in\mathcal{S}} \left| \sum_{k=0}^{N_{\text{obs}}-1} r^*(k/f_s) r\left(\frac{k + \lfloor f_s \psi_{\mu_1,\mu_2}^{-1}(u/f_s) \rceil}{f_s} \right) \times e^{-i2\pi\left(\alpha\psi_{\mu_1,\mu_2}(k/f_s) + 2\mu_2 u f_c k/f_s\right)} \right|^2, \tag{94}$$

where $\lfloor \cdot \rceil$ rounds towards the nearest integer (zero-order interpolation) so that (94) does not require any resampling. Similarly to the Doppler scale estimator, the maximization over μ_1 and μ_2 can be based on physical considerations of maximum velocity and acceleration.

REFERENCES

[1] F.-X. Socheleau, "Non data-aided estimation of time-varying multiscale doppler in underwater acoustic channels," in *Proc. Underwater Communications and Networking (UComms)*, 2021.

[2] W. A. Gardner, A. Napolitano, and L. Paura, "Cyclostationarity: Half a century of research," *Signal processing*, vol. 86, no. 4, pp. 639–697, 2006.

[3] W. A. Gardner, *Statistical Spectral Analysis: A Nonprobabilistic Theory, Part II, Periodic Phenomena*, Prentice-Hall, 1987.

[4] A. Napolitano, *Generalizations of cyclostationary signal processing: spectral analysis and applications*, vol. 95, John Wiley & Sons, 2012.

[5] A. Napolitano, "Cyclostationarity: New trends and applications," *Signal processing*, vol. 120, pp. 385–408, 2016.

[6] P. Cotae, Suresh R., and I. S. Moskowitz, "Non-data aided Doppler shift estimation for underwater acoustic communication," in *2014 10th International Conference on Communications (COMM)*. IEEE, 2014, pp. 1–6.

[7] B. Zhang, Y. Wang, H. Wang, L. Zheng, Z. Zhuang, and K. Xu, "Cyclic-feature based Doppler scale estimation for orthogonal frequency-division multiplexing (OFDM) signals over doubly selective underwater acoustic channels," in *Proceedings of Meetings on Acoustics*. Acoustical Society of America, 2017, vol. 30.

[8] Z. Wu and T.C. Yang, "Blind cyclostationary carrier frequency and symbol rate estimation for underwater acoustic communication," in *2012 IEEE International Conference on Communications (ICC)*. IEEE, 2012, pp. 3482–3486.

[9] Q. Li, X.and Han, Z. Liu, and Z. Wu, "Novel modulation detection scheme for underwater acoustic communication signal through short-time detailed cyclostationary features," in *2014 IEEE Wireless Communications and Networking Conference (WCNC)*. IEEE, 2014, pp. 624–629.

[10] P. A. van Walree and R. Otnes, "Ultrawideband Underwater Acoustic Communication Channels," *IEEE J. Ocean. Eng.*, vol. 38, no. 4, pp. 678–688, October 2013.

[11] F.B. Jensen, W.A. Kuperman, and B. Michael, *Computational ocean acoustics*, American Institute of Physics, New York, 1994.

[12] J. Bonnel, B. Nicolas, J.I. Mars, and S.C. Walker, "Estimation of modal group velocities with a single receiver for geoacoustic inversion in shallow water," *The Journal of the Acoustical Society of America*, vol. 128, pp. 719–727, 2010.

[13] F.-X. Socheleau, "CodeOcean capsule or github repository: Cyclostationarity of Communication Signals in Underwater Acoustic Channels [online]," 2022, https://codeocean.com/capsule/2187158, https://github.com/fxsocheleau/cyclostationarity-uac.

[14] M. Stojanovic, J. A. Catipovic, and J. G. Proakis, "Phase-coherent digital communications for underwater acoustic channels," *IEEE J. Ocean. Eng.*, vol. 19, no. 1, pp. 100–111, 1994.

[15] C. Laot and R. Le Bidan, "Adaptive MMSE turbo equalization with high-order modulations and spatial diversity applied to underwater acoustic communications," in *17th European Wireless 2011-Sustainable Wireless Technologies*, 2011, pp. 1–6.

[16] F. Frassati, C. Lafon, P.A. Laurent, and J.M. Passerieux, "Experimental assessment of OFDM and DSSS modulations for use in littoral waters underwater acoustic communications," in *Proc. IEEE Oceans'05*, Jun. 2005, pp. 826–831.

[17] T.C. Yang and W.-B. Yang, "Low probability of detection underwater acoustic communications using direct-sequence spread spectrum," *The Journal of the Acoustical Society of America*, vol. 124, no. 6, pp. 3632–3647, 2008.

[18] P. Otnes, R.and van Walree, H. Buen, and H. Song, "Underwater acoustic network simulation with lookup tables from physical-layer replay," *IEEE Journal of Oceanic Engineering*, vol. 40, no. 4, pp. 822–840, 2015.

[19] F.-X. Socheleau, M. Stojanovic, C. Laot, and J.-M. Passerieux, "Information-Theoretic Analysis of Underwater Acoustic OFDM Systems in Highly Dispersive Channels," *Journal of Electrical and Computer Engineering*, 2012, Article ID 716720.

[20] A. Bourré, S. Lmai, C. Laot, and S. Houcke, "A robust OFDM modem for underwater acoustic communications," in *2013 MTS/IEEE OCEANS-Bergen*. IEEE, 2013, pp. 1–5.

[21] S. Zhou and Z. Wang, *OFDM for underwater acoustic communications*, John Wiley & Sons, 2014.

[22] Y. V. Zakharov and A. K. Morozov, "OFDM transmission without guard interval in fast-varying underwater acoustic channels," *IEEE Journal of Oceanic Engineering*, vol. 40, no. 1, pp. 144–158, 2014.

[23] J. Potter, J. Alves, D. Green, G. Zappa, I. Nissen, and K. McCoy, "The janus underwater communications standard," in *2014 Underwater Communications and Networking (UComms)*. IEEE, 2014, pp. 1–4.

[24] H. Wang, O. A. Dobre, C. Li, and D. C. Popescu, "Blind cyclostationarity-based symbol period estimation for FSK signals," *IEEE Communications Letters*, vol. 19, no. 7, pp. 1149–1152, 2015.

[25] D. Vucic, "Cyclic spectral analysis of frequency hopping signals," in *2005 IEEE 16th International Symposium on Personal, Indoor and Mobile Radio Communications*. IEEE, 2005, vol. 2, pp. 1209–1213.

[26] F.-X. Socheleau, S. Houcke, P. Ciblat, and A. Aissa-El-Bey, "Cognitive OFDM system detection using pilot tones second and third-order cyclostationarity," *Signal processing*, vol. 91, no. 2, pp. 252–268, 2011.

[27] O. A. Dobre, R. Venkatesan, and D. C. Popescu, "Second-order cyclostationarity of mobile WiMAX and LTE OFDM signals and application to spectrum awareness in cognitive radio systems," *IEEE Journal of Selected Topics in Signal Processing*, vol. 6, no. 1, pp. 26–42, 2011.

[28] B. Tomasi, J. Preisig, G. B. Deane, and M. Zorzi, "A study on the wide-sense stationarity of the underwater acoustic channel for non-coherent communication systems," in *17th European Wireless 2011-Sustainable Wireless Technologies*. VDE, 2011, pp. 1–6.

[29] F-X. Socheleau, C. Laot, and J-M. Passerieux, "Parametric Replay-Based Simulation of Underwater Acoustic Communication Channels," *IEEE J. of Oceanic Eng.*, vol. 40, no. 4, pp. 4838–4839, 2015.

[30] P. A. van Walree, P. Jenserud, and M. Smedsrud, "A Discrete-Time Channel Simulator Driven by Measured Scattering Functions," *IEEE J. Sel. Areas Commun.*, vol. 26, no. 9, pp. 1628–1637, 2008.

[31] J. Li, Y. V. Zakharov, and B. Henson, "Multibranch autocorrelation method for Doppler estimation in underwater acoustic channels," *IEEE Journal of Oceanic Engineering*, vol. 43, no. 4, pp. 1099–1113, 2017.

[32] M. B. Porter, "The bellhop manual and user's guide: Preliminary draft," *Heat, Light, and Sound Research, Inc., La Jolla, CA, USA, Tech. Rep*, 2011.

[33] J. C. Preisig and G. B. Deane, "Surface wave focusing and acoustic communications in the surf zone," *The Journal of the Acoustical Society of America*, vol. 116, no. 4, pp. 2067–2080, 2004.

[34] A. Napolitano, "Time-warped almost-cyclostationary signals: characterization and statistical function measurements," *IEEE Transactions on Signal Processing*, vol. 65, no. 20, pp. 5526–5541, 2017.

[35] W. A. Gardner, "Statistically inferred time warping: extending the cyclostationarity paradigm from regular to irregular statistical cyclicity in scientific data," *EURASIP Journal on Advances in Signal Processing*, vol. 2018, no. 1, pp. 1–25, 2018.

[36] B.S. Sharif, J. Neasham, O.R. Hinton, and A.E. Adams, "A computationally efficient doppler compensation system for underwater acoustic communications," *IEEE J. Ocean. Eng.*, vol. 25, no. 1, pp. 52–61, 2000.

[37] Y. Zakharov, B. Henson, R. Diamant, Y. Fei, P. D. Mitchell, N. Morozs, L. Shen, and T. C. Tozer, "Data packet structure and modem design for dynamic underwater acoustic channels," *IEEE Journal of Oceanic Engineering*, vol. 44, no. 4, pp. 837–849, 2019.

[38] H.L. Van Trees, *Detection, Estimation, and Modulation Theory Part I*, Wiley, 1968.

[39] Y. Le Gall, F.-X. Socheleau, and J. Bonnel, "Matched-field processing performance under the stochastic and deterministic signal models," *IEEE Trans. Signal Process.*, vol. 62, no. 22, pp. 5825–5838, 2014.

[40] A. V. Dandawate and G. B. Giannakis, "Statistical tests for presence of cyclostationarity," *IEEE Transactions on signal processing*, vol. 42, no. 9, pp. 2355–2369, 1994.

[41] P. Jallon, "An algorithm for detection of DVB-T signals based on their second-order statistics," *EURASIP Journal on Wireless Communications and Networking*, vol. 2008, pp. 1–9, 2007.

[42] J. Lundén, S. A. Kassam, and V. Koivunen, "Robust nonparametric cyclic correlation-based spectrum sensing for cognitive radio," *IEEE Transactions on Signal Processing*, vol. 58, no. 1, pp. 38–52, 2009.

[43] A. Bouzegzi, P. Ciblat, and P. Jallon, "New algorithms for blind recognition of OFDM based systems," *Signal Processing*, vol. 90, no. 3, pp. 900–913, 2010.

[44] M. Kim, K. Po, and J. Takada, "Performance enhancement of cyclostationarity detector by utilizing multiple cyclic frequencies of OFDM signals," in *2010 IEEE Symposium on New Frontiers in Dynamic Spectrum (DySPAN)*. IEEE, 2010, pp. 1–8.

[45] J. A. Hildebrand, "Anthropogenic and natural sources of ambient noise in the ocean," *Marine Ecology Progress Series*, vol. 395, pp. 5–20, 2009.

[46] F Thomsen, S Mendes, F Bertucci, M Breitzke, E Ciappi, A Cresci, E Debusscher, C Ducatel, F Folegot, C Juretzek, et al., "Addressing underwater noise in Europe: Current state of knowledge and future priorities.," *EMB Future Science Brief*, vol. 7, 2021.

[47] X. Kuai, H. Sun, S. Zhou, and E. Cheng, "Impulsive noise mitigation in underwater acoustic OFDM systems," *IEEE Transactions on Vehicular Technology*, vol. 65, no. 10, pp. 8190–8202, 2016.

[48] A. Mahmood, M. Chitre, and H. Vishnu, "Locally optimal inspired detection in snapping shrimp noise," *IEEE Journal of Oceanic Engineering*, vol. 42, no. 4, pp. 1049–1062, 2017.

[49] T. E. Biedka, L. Mili, and J. H. Reed, "Robust estimation of cyclic correlation in contaminated gaussian noise," in *Conference Record of the Twenty-Ninth Asilomar Conference on Signals, Systems and Computers*. IEEE, 1996, vol. 1, pp. 511–515.

[50] S. A. Kassam, "Nonparametric signal detection," *Advances in Statistical Signal Processing*, vol. 2, pp. 66–91, 1993.

[51] F.-X. Socheleau, "Joint signal detection and channel estimation in multi-scale multi-lag underwater acoustic environments," in *Proceedings of Meetings on Acoustics UACE*. Acoustical Society of America, 2021, vol. 44.

[52] J. Bonnel, A. Thode, D. Wright, and R. Chapman, "Nonlinear time-warping made simple: A step-by-step tutorial on underwater acoustic modal separation with a single hydrophone," *The journal of the acoustical society of America*, vol. 147, no. 3, pp. 1897–1926, 2020.

[53] C.L. Pekeris, *Theory of propagation of explosive sound in shallow water*, vol. 27, Geol. Soc. Am. Mem., 1948.

[54] W. A. Gardner, "The spectral correlation theory of cyclostationary time-series," *Signal processing*, vol. 11, no. 1, pp. 13–36, 1986.

[55] R. S. Roberts, W. A. Brown, and H. H. Loomis, "Computationally efficient algorithms for cyclic spectral analysis," *IEEE Signal Processing Magazine*, vol. 8, no. 2, pp. 38–49, 1991.

[56] J. Antoni, "Cyclic spectral analysis in practice," *Mechanical Systems and Signal Processing*, vol. 21, no. 2, pp. 597–630, 2007.

[57] J. Antoni, G. Xin, and N. Hamzaoui, "Fast computation of the spectral correlation," *Mechanical Systems and Signal Processing*, vol. 92, pp. 248–277, 2017.

[58] F.-X. Socheleau, C. Laot, and J.-M. Passerieux, "Stochastic Replay of non-WSSUS Underwater Acoustic Communication Channels Recorded at Sea," *IEEE Trans. Signal Process.*, vol. 59, no. 10, pp. 4838–4849, 2011.

[59] R. Otnes, P. A. van Walree, and T. Jenserud, "Validation of Replay-Based Underwater Acoustic Communication Channel Simulation," *IEEE J. Ocean. Eng.*, vol. 38, no. 4, pp. 689–700, 2013.

[60] F-X. Socheleau, A. Pottier, and C. Laot, "Stochastic Replay of SIMO Underwater Acoustic Communication Channels," *OCEANS 2015*, pp. 1–6, October 2015.

[61] P. A. van Walree, F. X. Socheleau, R. Otnes, and T. Jenserud, "The watermark benchmark for underwater acoustic modulation schemes," *IEEE Journal of Oceanic Engineering*, vol. 42, no. 4, pp. 1007–1018, Oct 2017.

[62] "Sercel," https://www.sercel.com/.

[63] G. Real and D. Fattaccioli, "Acoustic coherence in a fluctuating ocean: analysis of the 2016 ALMA campaign," in *UACE 2017 Proceedings*, 2017.

[64] W. A. Gardner, "Cyclic wiener filtering: theory and method," *IEEE Transactions on communications*, vol. 41, no. 1, pp. 151–163, 1993.

[65] K. Abed-Meraim, Y. Xiang, J. H. Manton, and Y. Hua, "Blind source-separation using second-order cyclostationary statistics," *IEEE Transactions on Signal Processing*, vol. 49, no. 4, pp. 694–701, 2001.

[66] Y. Le Gall, F.-X. Socheleau, and J. Bonnel, "Performance analysis of single-receiver matched-mode localization," *IEEE Journal of Oceanic Engineering*, , no. 44, pp. 193–206, 2019.

[67] C. M. Spooner, *Higher-order statistics for nonlinear processing of cyclostationary signals*, IEEE Press New York, 1994.

[68] T. Fusco, L. Izzo, A. Napolitano, and M. Tanda, "On the second-order cyclostationarity properties of long-code DSSS signals," *IEEE Transactions on Communications*, vol. 54, no. 10, pp. 1741–1746, 2006.

[69] P. Ciblat, P. Loubaton, E. Serpedin, and G. B. Giannakis, "Asymptotic analysis of blind cyclic correlation-based symbol-rate estimators," *IEEE Transactions on Information Theory*, vol. 48, no. 7, pp. 1922–1934, 2002.

[70] L. Rabiner, R. Schafer, and C. Rader, "The chirp z-transform algorithm," *IEEE transactions on audio and electroacoustics*, vol. 17, no. 2, pp. 86–92, 1969.

[71] J. Barzilai and J. M. Borwein, "Two-point step size gradient methods," *IMA journal of numerical analysis*, vol. 8, no. 1, pp. 141–148, 1988.